Thesis for the Degree of Licentiate of Engineering

Design and Characterization of SiN-based integrated optical components for Wavelength Division Multiplexing

Alexander Caut

CHALMERS

Photonics Laboratory
Department of Microtechnology and Nanoscience - MC2
Chalmers University of Technology
Göteborg, Sweden, 2022

Design and Characterization of SiN-based integrated optical components for Wavelength Division Multiplexing
Alexander Caut
Göteborg, August 2022

Chalmers University of Technology
Microtechnology and Nanoscience - MC2
Photonics Laboratory
SE-412 96 Göteborg, Sweden
Phone: 07 64 22 54 97

ISSN 1652-0769
Technical Report MC2-455

Printed in Sweden by Reproservice, Chalmers University of Technology
Göteborg, Sweden, August 2022

Design and Characterization of SiN-based integrated optical components for Wavelength Division Multiplexing

Alexander Caut
Photonics Laboratory
Department of Microtechnology and Nanoscience - MC2
Chalmers University of Technology

Abstract

To follow the trend of the data traffic and to limit the size of the hyperscale data centers, communication solutions offering small footprint, low cost and low power consumption are needed. Optical interconnects used in data centers are mostly short reach (approximately 100 m) based on GaAs-based 850 nm vertical-cavity surface emitting lasers (VCSELs) and OM4 multimode fibers (MMF). However, with 1 km-long optical links, the use of VCSEL-MMF at 850 nm becomes challenging at high data rates (Tb/s) due to large modal dispersion and high propagation loss. Therefore, other cost-effective methods are needed to compensate these limits. Single mode GaAs-based VCSELs have been demonstrated at 1060 nm of wavelength, where the chromatic dispersion is lower, for optical links ranging between 300 m and 10 km. This solution could be a better alternative than InP-based distributed feedback laser sources at 1310 nm in terms of cost and energy dissipation. As the modulation bandwidth of GaAs-based single mode VCSELs is limited to around 30 GHz, reaching the capacity target then requires a wavelength division multiplexing scheme with parallel single-core fibers (SCFs) or even multi-core fibers (MCFs)

In this thesis we discuss different types of demultiplexers at 1060 nm of wavelength. The proposed designed demultiplexers are arrayed waveguide gratings (AWGs) and cascaded Mach-Zehnder interferometers (MZIs). These two technologies are compared in terms of transmission, bandwidth, crosstalk and footprint with the number of output channels. Grating couplers at 1060 and 850 nm for on-chip coupling are also studied. The goal is to couple the light coming from a single mode fiber or a VCSEL with the lowest possible loss and back reflection.

Keywords: arrayed waveguide gratings, Mach-Zehnder interferometers, insertion loss, crosstalk, grating couplers, power splitters, polarization, silicon photonics, silicon nitride.

Publications

This thesis is based on the work contained in the following papers:

[A] **Alexander Caut**, Marcello Girardi, Victor Torres-Company, and Magnus Karlsson, "Arrayed Waveguide Grating and MZI Filters for Wavelength Division (De-)Multiplexing at 1 μm", *In preparation.*

[B] Mehdi Jahed, **Alexander Caut**, Jeroen Goyvaerts, Marc Rensing, Magnus Karlsson, Anders Larsson, Gunther Roelkens, Roel Baets, and Peter O'Brien, "Angled Flip-Chip Integration of VCSELs on Silicon Photonic Integrated Circuits", in *Journal of Lightwave Technology (JLT)*, Vol. 40, No. 15, pp. 5190-5200, August 1, 2022. DOI: 10.1109/JLT.2022.3172781

Other publications by the author, not included in this thesis, are:

[C] A. S. Alam, M. Girardi, **A. Caut**, A. Larsson, V. Torres-Company, M. Galili, Y. Ding, and K. Yvind, "LiNbO3/Si3N4-Bilayer Vertical Coupler for Integrated Photonics", *CLEO 2020*

Contents

Acknowledgement

First, I would like to thank my supervisor Prof. Magnus Karlsson for giving me the opportunity to this adventure at the Photonics Lab, guiding me to the PhD and always keeping the door open when I have something I don't clearly understand. I would like to thank my co-supervisor Prof. Victor Torres-Company for his outstanding guiding through my research.

I would like to thank Marcello Girardi for teaching me how to use Lumerical and gdspy for the mask design. I thank him for helping me to familiarize with the characterization setup at the beginning of my PhD. He also deserves many thanks for all the time he spent in the cleanroom for manufacturing all the components I designed, no matter how big or difficult they were. I would like to thank Krishna Sundar Twayana for his explanations when I had trouble with the characterizations. Many thanks to Ekaterina Deriushkina for the amazing discussions during lunch time. I wish to thank Muhammad Bilal Aziz, Rasmus Larsson, Ali Mirani, Dr. Kovendhan Vijayan, Dr. Jochen Schröder and Prof. Peter Andrekson for helping me in the preparation of the laboratory exercises for the fiber optical communication course. I am thankful to Jeanette Träff for helping me in my first days in Sweden and to Gunnel Berggren for being so nice and and giving me weekly newspapers in Swedish to help me improve my knowledge of the language. I would like to thank everyone at the Photonics Lab for keeping it such a nice environment. I also wish to thank all my friends in Gothenburg who had made Sweden feel like my new home.

Last but not least, my deepest thanks go to my family. I want to express my profound gratitude to my parents for their love, support and care. I am also grateful to my little sister Chloé for bringing me joy through my research and for sharing her passions and thoughts.

Alexander Caut
Göteborg, August 2022

Acronyms

AWG	arrayed waveguide grating
MZI	Mach-Zehnder interferometer
GC	grating coupler
SMF	single-mode fiber
MMF	multi-mode fiber
CWDM	coarse wavelength-division multiplexing
DWDM	dense wavelength-division multiplexing
SNR	signal-to-noise ratio
BER	bit error rate

CHAPTER 1

Introduction

1.1 Network traffic

Global data traffic has been increasing at an exponential rate in the past decade. Mobile data traffic alone was 62 exabytes per month in 2020 and is expected to reach 607 exabytes in 2025 and 5016 in 2030 [1, 2]. While 5G technology is being released worldwide, 6G is already under development to meet the high demand for high-speed internet [2] and the main components of the internet infrastructure are optical cables and data centers. Data centers consist of a vast amount of servers where most of the world's data is stored and accessed. These servers require a substantial amount of power and cooling. According to an European Commission report, data centers consumed 2.7 % of electricity within the EU in 2018 and could reach 3.21 % in 2030 [3]. This is due to the growing size and number of data centers. The number of hyperscale data centers was 259 in 2015, 448 in 2018 and reached 700 at the end of 2021 [4]. The largest data center measures now 1 000 000 m^2 [5]. This means that to limit the increasing size of the hyperscale datacenters, interconnect solutions offering small footprint, low cost and low power consumption will be needed. Today's optical interconnects used in data centers are short reach and use standard GaAs-based 850 nm vertical-cavity surface emitting lasers (VCSELs) and OM4 multimode fibers (MMFs) [6–8]. At this wavelength, the fiber links typically reach distances of 100 m [9] at

data rates of 25 Gbps on-off keying (OOK) and 50 Gbps pulse amplitude modulation 4-level (PAM-4). However, in larger data centers with optical links of 1 km, the use of VCSEL-MMF at 850 nm becomes challenging at high data rates due to large modal dispersion and high propagation loss [7, 10]. Therefore, other methods are needed to overcome these limiting actions.

1.2 Motivation

The chromatic dispersion at 850 nm reaches -85 ps/nm/km in silica MMF and the propagation loss exceeds 2 dB/km [7, 10]. One possibility to reduce the chromatic dispersion effect consists in using single mode VCSELs as the bandwidth is much narrower than for multimode ones [7]. Moreover, single mode VCSELs reduce the impact of modal dispersion if launched into carefully selected mode groups of the MMF [7, 11]. Unfortunately, this also requires higher alignment precision [7]. However, the propagation loss is much lower for longer wavelengths (about 1 dB/km at 1060 nm and 0.4 dB/km at 1310 nm) and the chromatic dispersion is is also smaller (-25 ps/nm/km at 1060 nm and near 0 ps/nm/km at 1310 nm) [10]. 1060 nm single mode GaAs-based VCSELs have been demonstrated as a solution for optical links ranging between 300 m and 10 km [8]. As working at 1310 nm is an attractive alternative due to low chromatic dispersion and propagation loss, InP-based distributed feedback laser sources at 1310 nm have also been developed [6–8]. However, GaAs-based VCSELs proved to be more cost effective and more efficient in terms of energy dissipation [6] than the InP source at 1310 nm. Therefore, optical links at 1060 nm are desirable but to face the increasing demand for high interconnect capacity, the key challenge is reaching a capacity of several Tb/s [12]. As the modulation bandwidth of GaAs-based single-mode VCSELs is limited to around 30 GHz [12], reaching the capacity target then requires a wavelength division multiplexing scheme with parallel single-core fibers (SCFs) or even multi-core fibers (MCFs) [13, 14] as illustrated in Figure 1.1.

Figure 1.1 shows that a multi-wavelength GaAs-based VCSEL array is flip-chipped over a grating coupler on a photonic integrated circuit (PIC). The VCSELs are single-mode and their polarization must be stably aligned with the grating coupler [15, 16]. Moreover, the flip-chipped VCSELs are tilted to ensure low optical feedback [15]. Due to the limited gain bandwidth of the VCSELs, an array of 8 VCSELs will

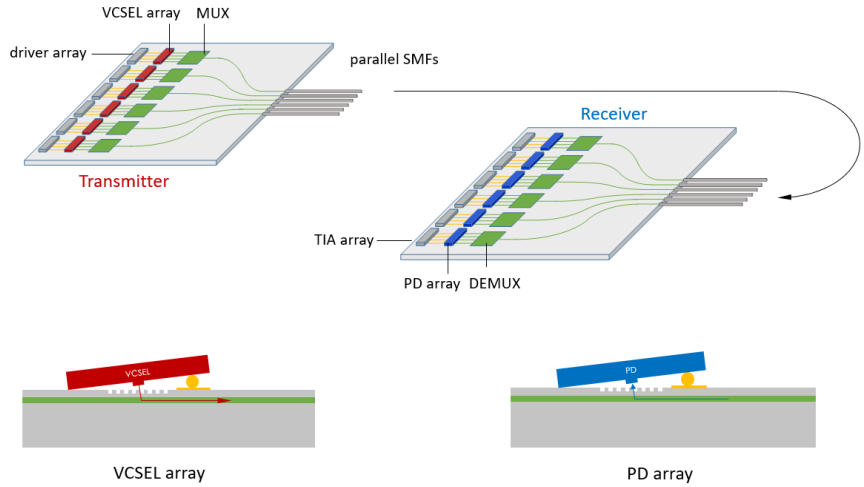

Figure 1.1: Short reach coarse wavelength-division multiplexing (CWDM) at 1060 nm. The light from the VCSEL array is coupled through grating couplers and guided to a multiplexer (MUX), a demultiplexer (DEMUX) and to an array of photodiodes (PD).

require a wavelength channel spacing of 4 nm whereas an array of 4 channels has a spacing of 8 nm [16]. To reduce the crosstalk, which is one of our key motivations, a 4-channel array with a 8 nm spacing is considered. The light from the VCSELs reaching the photodiode (PD) is coupled with a grating coupler for each channel. The PIC is made of silicon nitride (SiN) waveguides since SiN is compatible with complementary metal-oxide-semiconductor technology (CMOS). To ensure high data rate transmission to the PDs, the allowed loss budget for each optical component (VCSEL-grating coupler, MUX, waveguide-fiber coupler, fiber-waveguide coupler, DEMUX, grating coupler-PD) is 2 dB (Table 1.1). The VCSELs are emitting at center wavelengths 1023, 1031, 1039 and 1047 nm and Figure 1.2 shows the desired channel allocation for the CWDM. The minimum desired data rate with this setup is 1 Tb/s. This is possible by multiplexing the 4 wavelengths of the VCSEL arrays to 6 parallel single-mode fibers in a single optical cable, where each VCSEL provides a data rate 50 Gb/s using PAM-4 [8].

	Loss (dB)	Power (dBm)
VCSEL output		6
Grating coupler	2	4
MUX	2	2
Waveguide-fiber	2	0
Fiber-waveguide	2	-2
DEMUX	2	-4
Grating coupler	2	-6

Table 1.1: Power budget for each component. The VCSELs can deliver 6 dBm of power [8].

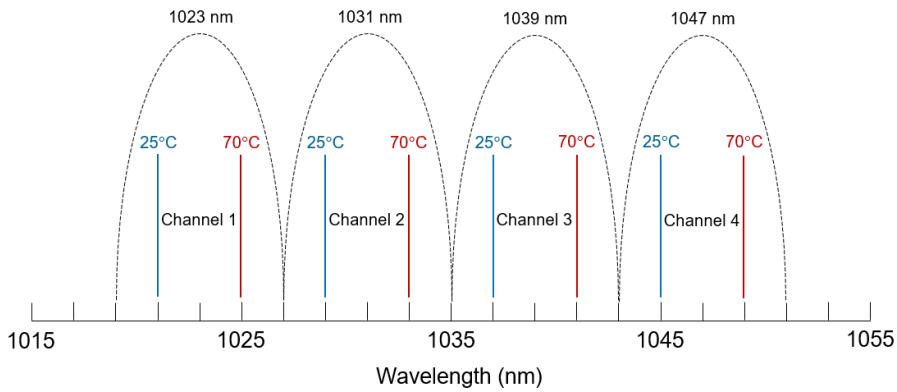

Figure 1.2: Channel allocation of the CWDM

1.3 This thesis

The focus of this thesis is on design, characterization and analysis of different types of multiplexers at 1060 nm of wavelength. The proposed multiplexers are (i) the arrayed waveguide gratings (AWGs) and (ii) the cascaded Mach-Zehnder interferometers (MZIs). In addition, we will also discuss grating couplers at 1060 and 850 nm. The papers that are included in this thesis emphasize AWGs and cascaded MZIs in terms of insertion loss, bandwidth and crosstalk (Paper [A]). It will be later extended for a deeper analysis on robustness of these two technologies to fabrication deviations (waveguide dimension, refractive index change), crosstalk, insertion loss, signal-noise-ratio (SNR), device's footprint with the number of channels and sensitivity to temperature compared to the VCSEL's temperature shift. Paper [B] is dedicated to Flip-chip VCSEL

over grating couplers at 850 nm of wavelength.

This thesis will first discuss in chapter 2 the different usable materials for the integrated optical waveguides, the simulation methods to estimate the insertion loss and also the different waveguide designs. Chapter 3 will focus on the different technologies for demultiplexing devices (AWGs, mircro-ring resonators, reflective AWGs...), then on design and analysis of AWGs and cascaded MZIs. Chapter 4 will present enhanced grating couplers at 1060 nm of wavelength and chapter 5 the future outlook of this thesis. Finally, chapter 6 outlines the main results and the included papers.

CHAPTER 2

Waveguide theory and simulation methods

Design of integrated photonic devices requires selection of the appropriate material and the waveguide geometry depending on the wavelength and the device requirements. Indeed, the waveguide material will have an impact on the mode confinement, the device's footprint and the waveguide dimensions. The waveguide is either sandwiched between cladding layers made of silica for good mode confinement or just deposited on top of a silica cladding layer. For good mode confinement, the core index must be larger than the cladding index. The most commonly used waveguide materials in silicon photonics are silicon, silicon nitride and silica.

2.1 Waveguide materials

2.1.1 Silicon waveguides

Silicon (Si) is a material that is CMOS-compatible, which is important for semiconductor devices. Due to high refractive index contrast between silicon and silicon dioxide (SiO_2), the mode confinement in the waveguide is excellent, allowing ultra-short bending radius (a few micrometers) and thus small footprint. However this also leads to strong roughness of waveguide sidewalls and higher scattering loss [17]. Si-waveguides are mostly based on silicon-on-insulator (SOI) platform. In addition, the Si material has low absorption in the wavelength range 1.1-8.5 μm,

which means this material cannot be used for optical interconnects with wavelengths shorter than 1.1 μm (for example 850 nm) [18]. Finally, Si waveguides have an effective index that is very sensitive to waveguide width variation. Indeed, multiplexers (AWGs, MZIs) made of Si waveguides show a shift of 1 nm in the center wavelength for a 1 nm waveguide width dimension [18]. As we want to make robust designs to any fabrication deviation, this material was less suitable for our devices.

2.1.2 Silicon nitride waveguides

Silicon nitride (SiN) waveguides make a good alternative to waveguides made of silicon. Also being a CMOS-compatible material, the refractive index of Si_3N_4 being around 2.00 at 1050 nm of wavelength, the refractive index contrast between the SiO_2 cladding and the waveguide is thus much smaller. This decreases the sensitivity of scattering loss due to sidewall roughness. Silicon nitride can be deposited either in low-pressure chemical vapor deposition (LPCVD) at 700°C, in plasma enhanced chemical vapor deposition (PECVD) at 400°C [17] and also with sputtering. The LPCVD deposition method has the advantage of keeping control of the SiN stoechiometry and is most suited for the telecom band (1550 nm) [17], and also in the 1 μm band. Moreover, SiN can be used for wavelengths much shorter than 1.1 μm as opposed to Silicon, and varying the N/Si ratio can cover wavelengths close to 400 nm [18]. The SiN waveguide is deposited with LPCVD in Paper [A] and PECVD in Paper [B] (at 850 nm of wavelength). The drawback of SiN is that its lower refractive index leads to lower mode confinement, which prevents small bending radius in curved waveguides and increases the device's footprint. However, this is largely compensated by the ultra-low propagation loss obtained in SiN waveguides, which is the priority of our research. Therefore, SiN was selected for fabrication in the cleanroom and platform development.

2.1.3 Silica waveguides

Silica (SiO_2) is another interesting alternative to silicon for wavelengths shorter than 1.1 μm. Due to low index contrast between the core and the cladding (also made of silica), the waveguide dimensions can almost match the fiber's core, enabling ultra low fiber-chip coupling loss (0.1 dB) [18]. In addition, this material can provide low propagation loss (0.017 dB/cm for a 7 μm x 7 μm waveguide) [18]. Nevertheless, the

extremely low contrast between the core and the cladding will require ultra-large bending radii (up to tens of millimeters) and thus to large size [18].

2.2 Waveguide geometries

2.2.1 Designs

The most common waveguide for telecommunication is the optical fiber which consists of a circular core made of silica surrounded by a circular silica cladding. The relative refractive index difference between the core and the cladding is circa 0.01, the core index being greater than the cladding index. However, for optical integration, the waveguide geometry needs to be adapted to layer deposition which is planar. Therefore, the waveguide designs are rectangular and the two main geometries are the strip and the rib waveguides as illustrated in figure 2.1. The core materials used were discussed in the previous section (silicon nitride is chosen here) and the cladding is silica. Thick waveguides surrounded by cladding allows strong confinement of the optical mode in both transverse and horizontal directions.

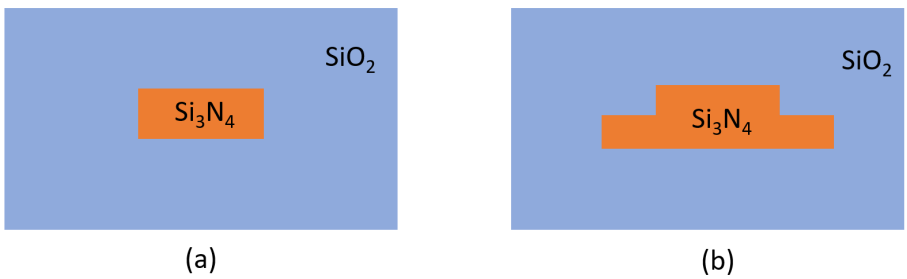

Figure 2.1: Scheme of (a) strip and (b) rib waveguide.

The strip waveguide requires only one etching step whereas the rib waveguide requires two steps [19]. Moreover, the strip geometry allows smaller bending radius, which reduces the device footprint. However, the main source of propagation losses is the roughness on the waveguide sidewalls and the rib design has lower sidewalls compared to the strip design for the same geometry [19]. This makes the rib design interesting for devices based on thick waveguides (740 nm thick for SiN at 1550 nm of wavelength). The waveguide confinement factor represents how well the electromagnetic field is confined in the core and can be defined as

the ratio of the electromagnetic fields within the core area to the electromagnetic fields within the full structure (top and bottom claddings included) [20–22]. Therefore, a thick waveguide will have a larger confinement factor than a thin waveguide.

2.2.2 Mode propagation and polarizations

The guided mode in the waveguide has a parameter called effective index denoted n_{eff}, given by

$$n_{eff} = \frac{\beta}{k_0}, \tag{2.1}$$

where β is the waveguide propagation constant and $k_0 = \frac{2\pi}{\lambda_0}$ the wavenumber with λ_0 being the wavelength of light in vacuum. The condition on the effective index for the optical mode to be guided in the waveguide is $n_{cl} < n_{eff} < n_c$, n_{cl} being the cladding index and n_c the core index. Fig. 2.2 shows an example of the simulated mode field profiles in the two polarization states (in the case of a single mode waveguide at 1550 nm of wavelength). The waveguide in the simulation is SiN and the cladding is SiO_2. There are two polarization states possible for the mode field: the TE polarization state in which the electric field is in the y-direction (fig. 2.2.a) and the TM polarization state in which the electric field is in z-direction (fig. 2.2.b).

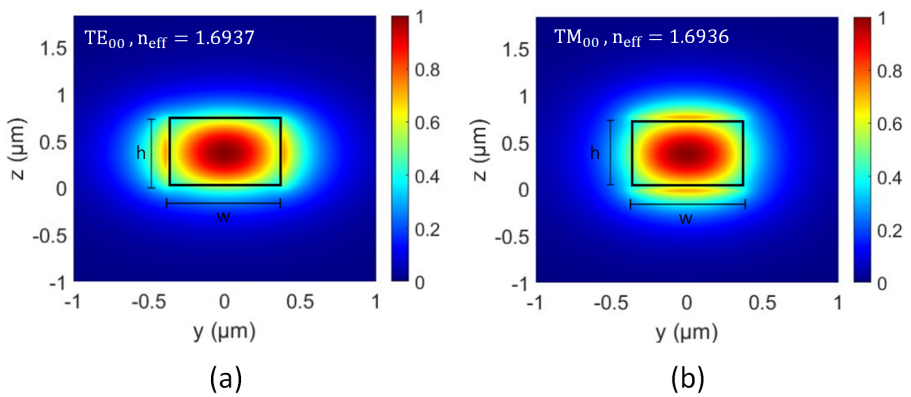

Figure 2.2: Mode field profiles of (a) TE_{00} and (b) TM_{00} modes (h = 740 nm, w = 740 nm) at 1550 nm of wavelength.

The waveguide is square-shaped and is 740 nm thick and 740 nm wide. Therefore the fundamental TE and TM modes have almost the

same effective indices ($n_{eff,\ TE00} = 1.6937$ and $n_{eff,\ TM00} = 1.6936$). The simulations are carried out in lumerical FDE (Finite Difference Eigenmode). Even though the waveguide is square-shaped, the effective indices of the TE_{00} and TM_{00} slightly differ due to the anti-symmetry of the simulation region. Indeed, the different layers of SiO_2 (thermal, LPCVD and PECVD) are also taken in account, each one having different refractive indices. As the modes are well confined in thick waveguides, low bending radius can be achieved with low loss. In addition, thick waveguides can achieve low polarization sensitivity as shown in the simulations. However, thick waveguides need to have a reduced width in order to be single mode. As a result, the modes shown in Figure 2.2 have a strong interaction with the sidewalls, leading to higher radiation loss due to roughness [23]. One possibility to reduce the mode interaction with the sidewalls consists in increasing the waveguide's width. Unfortunately, the waveguide would then become multimode as higher-order modes can be excited [24] and propagate through the cascaded devices in a photonic integrated circuit, thus spoiling the signal. Therefore, there is a tradeoff between strong-confinement SiN waveguides and single mode behaviour. This tradeoff consists in making the waveguide sufficiently large to minimize the mode interaction with the sidewalls and also thin enough to ensure a single mode behaviour. Fig. 2.3 shows the simulation of the mode field profiles for a 200 nm thick and 1500 nm wide waveguide, at the same wavelength.

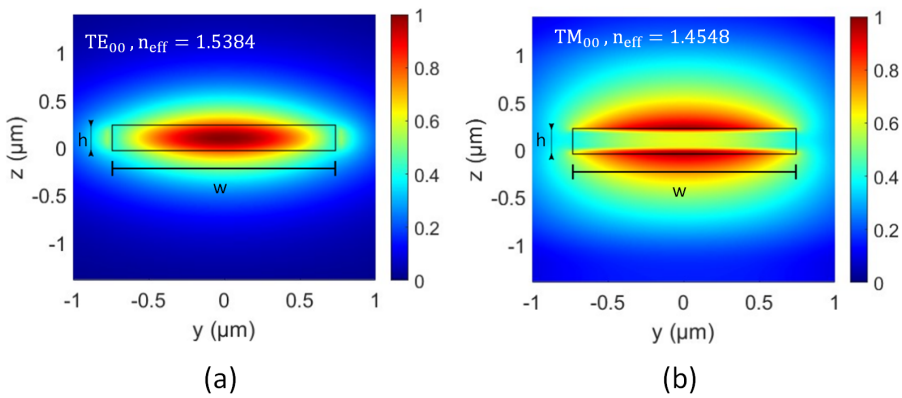

Figure 2.3: Mode field profiles of (a) TE_{00} and (b) TM_{00} modes (h = 200 nm, w = 1500 nm) at 1550 nm of wavelength.

The simulations show that mode confinement is more moderate when

looking at the effective index values. The fundamental TE_{00} mode is more confined than the TM_{00} mode ($n_{eff,\ TE00} = 1.5384 > n_{eff,\ TM00} = 1.4548$). As the waveguide is thin and rectangular-shaped, the modes are much less confined than in the square-shaped waveguide in fig. 2.2. This generally results in higher radiation losses in bent waveguide sections which have to be compensated with larger bending radius (thus increasing the size of the device). As the TE mode is more confined than the TM mode and thus less lossy, this is why the TE polarization state is preferred in integrated optics.

In the next chapters, the fabricated devices we are going to explore will be based on thin waveguides (around 160-170 nm thick and 900 nm wide) and the center wavelength at 1035 nm.

2.3 Simulation methods

This section introduces the different simulation methods (FDTD, varFDTD and EME) and explains which method is the most suitable depending on the optical device.

2.3.1 FDTD solver

The FDTD solver simulates the whole device by solving the Maxwell equations on a discrete spatial and temporal grid. The entire structure is divided into multiple cells and the different field components (Ex, Ey, Ez, Hx, Hy and Hz) are solved for each cell. It can simulate 3D photonic structures such as grating tapers, tapers, Y-splitters and multimode interferometers (MMIs). However, the computing time increases exponentially with the size of the device. Therefore this solver is used to simulate small devices in 3 dimensions (typical size: 20 μm x 40 μm x 1.5 μm) such as grating couplers, or other devices with bent structures (Y-splitters, directional couplers). Moreover, FDTD has the advantage of capturing all the relevant wavelengths within a few minutes. Finally, the simulation accuracy and computation time are increased when reducing the size of the cells.

2.3.2 varFDTD solver

The varFDTD solver basically collapses a 3D-FDTD simulation into an efficient 2D-FDTD simulation (often referred as 2.5D-FDTD), thus

significantly reducing memory requirements and computing time compared to pure FDTD. This solver can thus simulate much bigger devices than a conventional 3D-FDTD simulation (size: 1000 μm x 400 μm). However, this method assumes that there is no coupling between the slab modes guided in the vertical waveguide structure, or no polarization conversion [25]. Thus this method is efficient for planar and wide structures. Typical devices that can be simulated with varFDTD are as ring resonators, multi-mode interferometers (MMIs), directional couplers (DCs) or Mach-Zehnder interferometers (MZIs). Nevertheless, convergence testings are necessary to increase the simulation accuracy and, depending on the size of the device, careful checks can be made with either 3D-FDTD or EME simulations for result verifications.

2.3.3 EigenMode Expansion (EME) solver

EME is a frequency domain method that consists in bi-directionally propagating the device to calculate the final S matrix. This simulation method is adapted for straight continuously varying structures such as tapers or MMIs. The first step of the EME solver consists in dividing the device structure in a set of cells. Then the solver requires the selection of the number of propagating modes for each defined section of the device. Finally, the propagating mode for each input/output port of the device are bi-directionally propagated through the device. The first advantage of the EME solver over FDTD is that it only needs one cell to simulate a rectangular region (for example the rectangular region of the MMI). The second advantage is when in analysis mode, the solver can scan the length of a tapered structure with hundreds of simulations in a few minutes. For comparison, this step with FDTD would take several hours to realize only a few simulations. In analysis mode, the solutions to each section is bi-directionally propagated to calculate the S matrix of the entire device. This method is extremely efficient as it allows the calculation of the optimal length of the device. To increase the simulation accuracy, the number of propagating modes needs to be increased.

2.3.4 Summary

The running time of the different solvers and a few example devices are summarized in table 2.1. The grating coupler, MMI, directional coupler and the MZI have a size of respectively: 16 μm x 35 μm, 8 μm x 110 μm, 80 μm x 200 μm (bent waveguides included) and 700 μm x 200 μm.

Concerning the MMI, the EME solver will find the optimal length of the rectangular region much faster than the other methods.

	Grating coupler	MMI	Directional coupler	MZI
FDTD	4 min(2D), 2 h(3D)	1 h	1 h	60 h
varFDTD	N.A.	4 min	4 min	30 min
EME	N.A.	$<$ 4 min	N.A.	N.A.

Table 2.1: Solvers running times for different kind of devices

CHAPTER 3

Demultiplexing technologies for coarse wavelength-division multiplexing (CWDM)

This chapter explores the different demultiplexing technologies and expands the results in Paper [A]. It presents the design steps of the chosen technologies which are the arrayed waveguide grating (AWG) and the cascaded Mach-Zehnder interferometer (MZI). Then, in the last part, it compares them in terms of fabrication tolerance, refractive index change, signal flatness, sensitivity to temperature and footprint. The wavelength is centered at 1035 nm and the waveguide is 160 nm thick and 900 nm wide to ensure a single mode waveguide.

3.1 Types of wavelength division (de-)multiplexers

In this section, we will review different types of demultiplexers. Their insertion loss, crosstalk level, fabrication tolerance and footprint will be discussed. Then we will explain which devices were selected for CWDM at 1 μm of wavelength.

3.1.1 Arrayed waveguide gratings

An AWG consists of a set of arrayed waveguides connecting two free propagation regions (FPRs), input waveguides linked to the first FPR and output waveguides to the second as shown in Figure 3.1. AWGs are

attractive due to their potentially small footprint and to the low insertion loss and low crosstalk level they can provide.

The arrayed waveguides connecting the FPRs have a constant length increment. The light coming from the first FPR propagates through the arrayed waveguides in which each wavelength undergoes a phase shift provided by this length increment. The phase shift $\Delta\Phi_n$ of the n^{th} arrayed waveguide is linearly dependent on the frequency ν and is given by $\Delta\Phi_n = 2\pi n_c \nu l_n / c$, where c is the speed of light in vacuum, n_c the effective index of the arrayed waveguides and l_n the length of the n^{th} arrayed waveguide. Finally, the wavelengths will interfere constructively in the second FPR and focus at the output waveguides. The free spectral range (FSR) is set by the length difference between the arrayed waveguides [26]. In addition, the receiver and arrayed waveguide separations and the FPR length set the channel spacing [26].

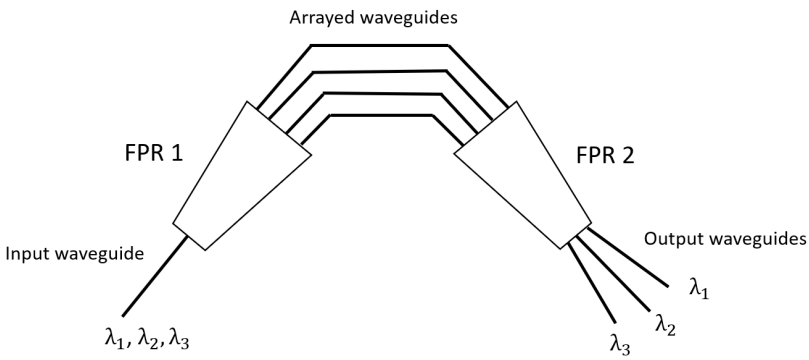

Figure 3.1: Illustration of an AWG

One particular advantage of AWGs is their flexibility about the possibility to insert several input waveguides since they are not on the same side than the output waveguides. Indeed, hitting the target wavelength might be a difficult task and there is usually a shift between simulations and measurements. Therefore, if the light is sent through another input waveguide along the Rowland circle [27] of the first FPR, the device's spectra can be shifted. Finally, AWGs are dominant in dense wavelength-division multiplexing (DWDM) due to the high number of channels required, their flexibility and footprint and low fabrication constraints. Typical AWGs can support 32 channels spaced at 100 GHz apart (0.8 nm) within the c-band spectrum (1550 nm) [28]. Large scale

25-GHz-spacing 400-channel AWGs have also been developed [29]. However, as the device's footprint increases with the number of channels, other technologies were developed. An AWG with overlapping FPRs was demonstrated in [30]. It is also possible to flatten the device's frequency response by inserting a multi-mode interferometer at the input waveguide, but then at the cost of higher insertion losses [31, 32]. The AWG is one of our selected technology for wavelength division multiplexing.

3.1.2 Reflective arrayed waveguide gratings

One way to reduce the AWG footprint consists in removing one FPR and using a reflective structure in the arrayed waveguide section. The AWG's footprint is then reduced by a factor of 2. As opposed to conventional AWGs, a RAWG has the input waveguide on the same side as the output waveguides. The arrayed waveguides start from the FPR and are ended with either conventional mirrors or with photonic crystal reflectors. However, dielectric or metal films are required for conventional mirrors and the cleaved facets need to be critically smoothed [30, 33] and photonic crystal structures also make the fabrication more challenging [34].

3.1.3 Echelle diffraction gratings

An EDG consists of an FPR with a reflection grating on one side and, on the other side one input and several output waveguides. This device provides low insertion loss and good crosstalk levels (below -20 dB) [30]. The phase delay is provided by the facets of the device. Moreover, the insertion loss can be further improved by adding Bragg mirrors at the facets [30]. The EDG's footprint can be smaller than the AWG's in CWDM. However, in DWDM the AWG can be smaller than the EDG [35]. In addition, this type of device requires smooth and deeply etched grating facets to limit excess loss [30, 36] and the input waveguide is situated on the same side of the output waveguides, limiting its flexibility compared to the AWG.

3.1.4 Cascaded Mach-Zehnder interferometers

Cascaded MZIs are another type of demultiplexing devices and consist of cascaded filters which are composed of two power splitters connected by an upper and lower arm, with a path length difference. The power splitters are either directional couplers (DC) or multi-mode interferometers (MMIs). MZI filters have the advantage of being easy to design

and to manufacture, which make them a good alternative to AWGs in CWDM. However in DWDM, when the number of channels exceeds 4, the MZI becomes larger than the AWG. In addition, this type of device provides low insertion loss [37,38] and low crosstalk level can be achieved with either stage doubling [38, 39] or with MMIs as shown in Paper [A]. Thus, this device was selected in addition to the AWG for comparison.

3.1.5 Cascaded multimode waveguide gratings

Cascaded multimode waveguide gratings (MWG) are basically contra-directional grating coupler-based devices. The major advantage of grating-based devices is the reduced footprint [38]. The input light source is directed to a multimode waveguide section and into a grating where the desired wavelength is coupled back into an output single mode waveguide. Previous works demonstrated four-channel CWDM cascaded MWG in the O-band (1240-1360 nm) with channel spacing of 20 nm, insertion loss below 1 dB and crosstalk level below -20 dB [40]. However, this kind of technology requires strong grating apodization to achieve low level crosstalk and strong corrugation depth to obtain flat-top channel response [40, 41].

3.1.6 Microring resonators

Microring resonators (MRR) are similar to MWGs and could constitute a nice alternative to AWGs. Indeed AWGs can suffer from random phase errors due to deviation from fabrication [42] and MRRs have the potential of being compact, and in addition having low loss. However, multi-microrings are necessary to achieve flat-top response and low crosstalk level [43], thus increasing the sensitivity to fabrication inaccuracies [44].

3.2 Power splitters

This section focuses on two kinds of power splitters used in cascaded MZIs, namely the MMI and the directional coupler.

3.2.1 Multimode interferometers (MMIs)

The stucture of a MMI consists of a group of input/output single mode waveguides and a wide multimode waveguide in the middle. This type of device has the advantage of being broadband and tolerant to fabrication deviations [45]. The input field comes from one of the two input waveguides and propagates through the multimode section. Imaging of the input field can be achieved when the length of the device is set as shown in Figure 3.2 [46]:

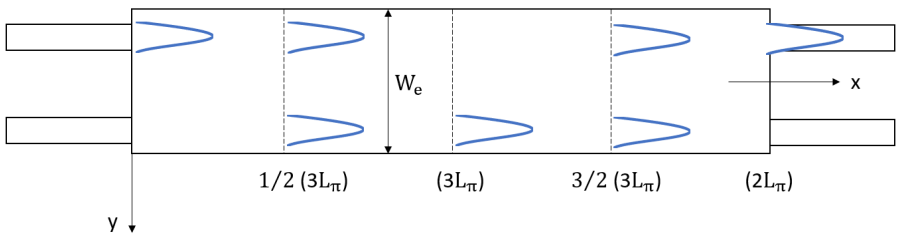

Figure 3.2: Field pattern (represented in blue) in a 2 x 2 MMI when the light comes from the upper input waveguide.

L_π is the beat length of the two lowest order modes in the MMI section and is given by [31]:

$$L_\pi = \frac{4 n_r W_e^2}{3\lambda_0}, \tag{3.1}$$

where n_r is the refractive index of the waveguide, W_e the effective width of the MMI and λ_0 the wavelength. When the length L of the multimode section is set as $L = 3/2\ L_\pi$, double imaging of the input field is realized with a loss of 3 dB for both output fields [46]. This is the length we want to select for our device to obtain a 3 dB coupler. A scheme of the designed MMI in Paper [A] is presented in Figure 3.3.

The example manufactured and discussed in Paper [A] is a 2 x 2 MMI (two input and two output waveguides) and consists of a $W = 8$ μm wide and $L = 70$ μm long slab-waveguide. The input and output waveguides are spaced by $W/3$ and are linearly tapered to reduce the

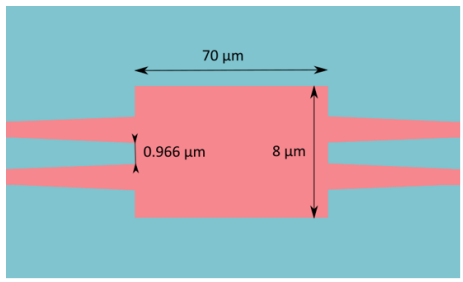

Figure 3.3: Illustration of the designed 2 x 2 MMI.

insertion loss introduced by the device [38]. However, these devices are difficult to design for arbitrary cross coupling coefficients [38]. The device was designed with Mode-solution Lumerical software, using both EME and varFDTD solvers. The results of the simulations are shown in Figure 3.4.

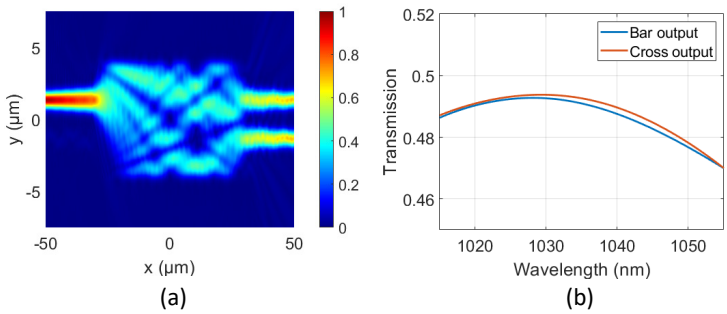

Figure 3.4: (a) varFDTD simulated power distribution of the MMI for the TE mode. (b) Transmission of the MMI. The 'Bar' and 'Cross' outputs are respectively the upper and lower outputs when the upper input is selected.

3.2.2 Directional couplers (DCs)

The DC can be described as a set of two parallel waveguides enabling the transfer of light from one waveguide to the other through evanescent coupling. The device is characterized by 4 ports (2 inputs and 2 outputs) and a straight section in which the light coupling occurs. DCs are attractive due to their low insertion loss, compactness and are easy to design for arbitrary cross coupling coefficients. The main characteristics that determine the cross coupling coefficient are the waveguide dimensions,

the gap between the waveguides in the straight section and the length of the latter. However, straight DCs are more wavelength dependent than MMIs [38] and less tolerant to fabrication deviations. In Paper [A], three DCs were designed for following cross coupling coefficient: K = 0.5, 0.29 and 0.08 [32, 37]. The length L of the straight section and the gap g between the waveguides were L = 20 μm and g = 300 nm for K = 0.5, L = 13 μm and g = 300 nm for K = 0.29, L = 13 μm and g = 440 nm for K = 0.08. The field profiles and the transmissions of the DCs are shown in Figures 3.5 and 3.6.

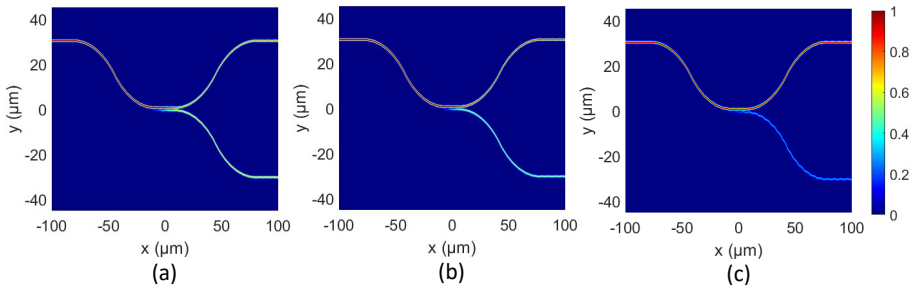

Figure 3.5: varFDTD simulated power distribution of the DC for K = (a) 0.5 (b) 0.29 (c) 0.08 for the TE mode.

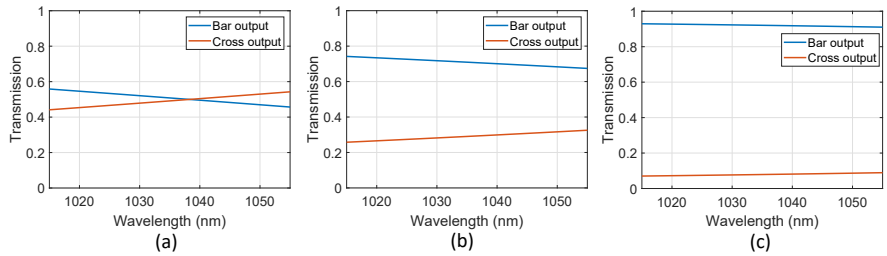

Figure 3.6: Transmission of the DC for K = (a) 0.5 (b) 0.29 (c) 0.08.

3.3 Design of components

3.3.1 Design of AWGs

The AWG design in this thesis is conventional. For both FPRs of the device, the input and arrayed waveguides are separated by a distance of respectively d_r and d_a along the FPR as illustrated in Figure 3.7. As explained in section 3.1, the different parameters set the FSR and the wavelength channel spacing.

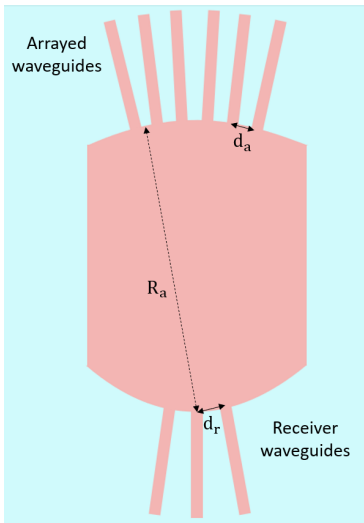

Figure 3.7: Scheme of the AWG star coupler

With the input and output star couplers of the AWG being identical, the following conditions should be satisfied [47]:

$$\beta_c(\lambda_0)\Delta L = 2m\pi, \tag{3.2}$$

$$\lambda_0 = \frac{n_c \Delta L}{m}, \tag{3.3}$$

where β_c is the propagation constant in the FPR regions, m the diffraction order of the AWG, ΔL the length increment between the array waveguides, n_c the effective index of the arrayed waveguides, λ_0 the central wavelength. The the free spectral range (FSR) in the frequency domain is related to the diffraction order m of the AWG with following equation [26]:

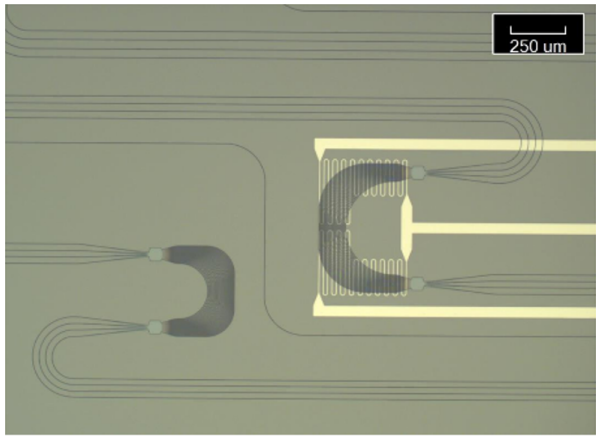

Figure 3.8: Microscope image of 4-channel AWGs with a reference waveguide between the two devices. The right AWG is equipped with a thermal heater to tune the channel wavelengths. In addition, we put 4 input waveguides on the first star coupler so we can shift the overall transmission in case it is not centered at 1035 nm.

$$\mathrm{FSR} = \frac{\nu_0}{\mathrm{m}}, \tag{3.4}$$

where ν_0 is the center frequency. To maintain a low loss non-uniformity for the outer channels, the FSR in the wavelength domain should at least be equal to Nx$\Delta\lambda$ [48], where N is the number of channels and $\Delta\lambda$ the channel spacing. Then with the combination of equations 3.3 and 3.4, we can deduce the length increment as a function of the FSR in the frequency domain:

$$\Delta\mathrm{L} = \frac{\mathrm{c}}{\mathrm{n_c FSR}}, \tag{3.5}$$

where c is the vacuum speed of light. The central wavelength, wavelength channel spacing and the FSR are set before designing the device. In Figure 3.8 is shown a microscope image of manufactured AWGs for CWDM. The main parameters are found with commercial WDM Phasar software and the mask design is later done with python. To prevent phase errors due to different bending radius in the array of conventional AWG designs [27], identical bends across the entire array section is applied in these devices.

3.3.2 Design of cascaded MZIs

The cascaded MZI consists of three filters cascaded in two stages as shown in Figure 3.9 when the device has 4 channels. The first stage separates the odd from the even wavelengths and also determines if the MZI response will be either Gaussian or flat-top. A first order filter in Stage 1 leads to a Gaussian response and a second order filter leads to a flat-top response. For a Gaussian MZI filter, only power splitters with a cross coupling coefficient K = 0.5 is necessary. However, to obtain a flat-response, cross coupling coefficients of K = 0.5, 0.29 and 0.08 (for a second order filter) are required [32, 37]. The two MZI orders are presented in Figure 3.10.

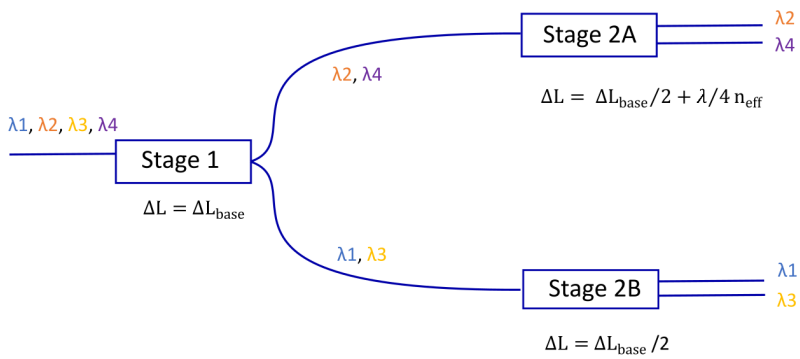

Figure 3.9: Diagram of a cascaded MZI. λ is noted as the center wavelength.

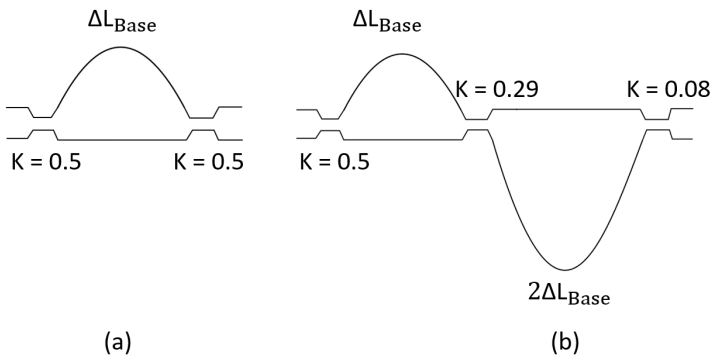

Figure 3.10: Schemes of first order (a) and second order (b) MZI filters. The K coefficients refer to the cross coupling coefficients of the directional couplers (or MMIs).

The free spectral range (FSR) is determined by the central wavelength λ, the waveguide group index n_{gr} and the base length difference ΔL as [49]:

$$FSR = \frac{\lambda^2}{n_{gr}\Delta L}. \tag{3.6}$$

The base length difference for the first stage of the cascaded MZI can be deduced by [49] ($\delta\lambda$ being the channel spacing):

$$\Delta L_{Base} = \frac{\lambda^2}{2\delta\lambda n_{gr}}. \tag{3.7}$$

Each stage is then simulated separately. The first has a FSR of 16 nm and the second a FSR of 32 nm. The calculated base length difference is around 35.76 μm for the first stage and 17.88 μm for the second (an additional shift is necessary for the stage 2A in Fig. 3.9). Figs. 3.11 shows the simulations for each stage when the used power splitters are directional couplers.

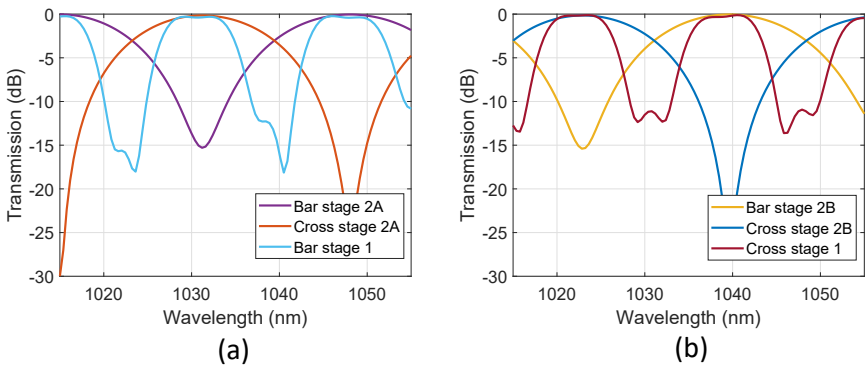

Figure 3.11: Simulation of (a) the upper arm MZI filter (Stage 2A) and (b) the lower arm MZI filter (Stage 2B)

The simulations reveal the high crosstlalk level (around -12 dB) of the flat-top MZI in the first stage when using straight directional couplers for all cross coupling coefficients. This is due to the high wavelength sensitivity of the straight directional couplers [38] as reported earlier. The use of broadband bent-directional couplers [32,38] or MMIs [38] can significantly reduce the crosstalk level.

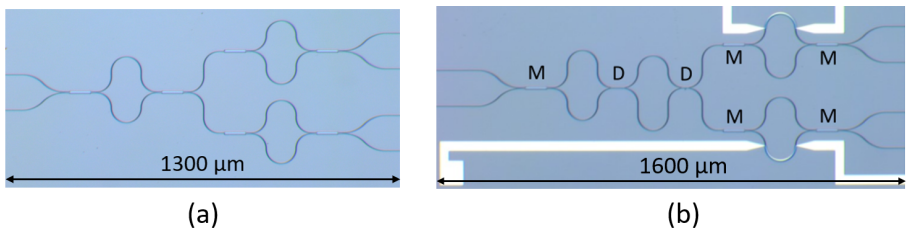

Figure 3.12: Microscope image of manufactured 4-channel cascaded Gaussian MZI (a) and flat-top MZI (b). The "M" and "D" letters refer to MMIs and DCs respectively.

3.4 CWDM at 1 μm

In this section, the waveguide dimension is set to be 160 nm thick and 900 wide. The desired channel spacing is 8 nm (4 channels) and the center wavelength is 1035 nm. The goal is to compare the AWG with the cascaded MZI. For the MZI filters, the MMI was selected as power splitter for the cross coupling coefficient K = 0.5 as it is less sensitive to fabrication deviation than directional couplers [8] and also less wavelength sensitive [38]. However, as the MMI introduced additional losses for K = 0.29 and 0.08, we used directional couplers instead for these coefficients. We compare in this section the signal flatness, the bandwidth, insertion loss, crosstalk, channel accuracy when one of the waveguide dimension shifts by a few nm and when the refractive index changes (by 0.1 %), the footprint when increasing the number of channels and finally sensitivity to temperature.

3.4.1 Transmitted power

Both devices were simulated as shown in Figure 3.13. The VCSEL can hit the target wavelength with a measured accuracy of ±3.1 nm (plotted in dashed lines below). The difference between the Gaussian and flat-top AWG is that for the input star coupler, the Gaussian AWG is equiped with input 400 μm long linear tapers whereas the flat-top AWG has 17 μm parabolic tapers [31]. For the Gaussian cascaded MZI, the first stage is a first order filter and for the flat-top design, it is a second order one.

In the case of the Gaussian AWG (Figure 3.13 (a)), when channel no. 4 perfectly hits the target wavelength (1047 nm), the corresponding VCSEL can deviate in the worst case by 3.1 nm and the insertion loss is 10 dB whereas it is only 0.5 dB for the Gaussian cascaded MZI (Figure

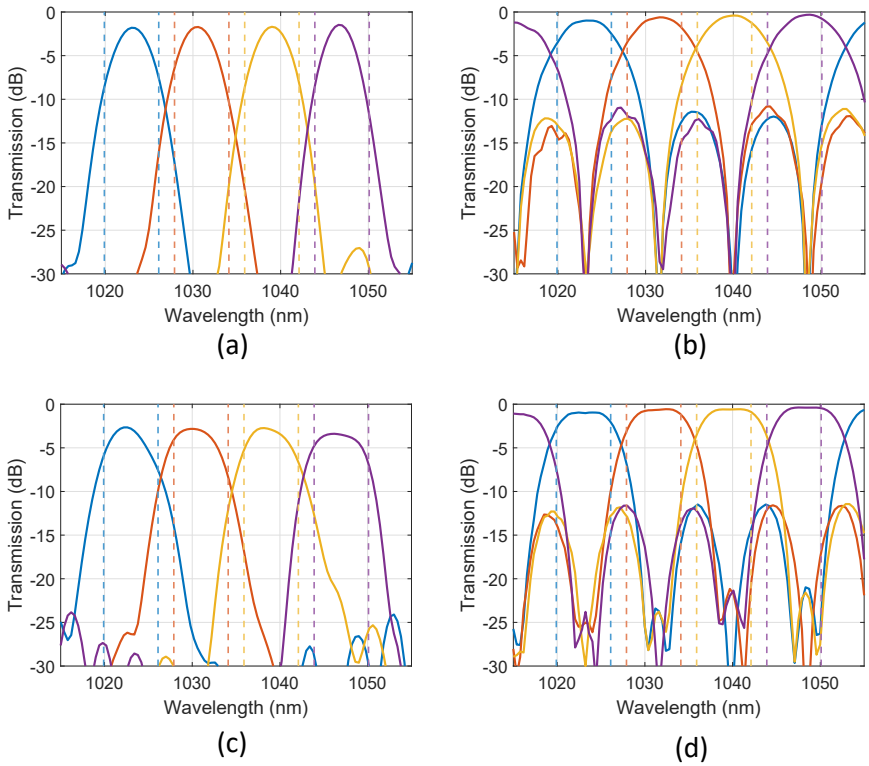

Figure 3.13: Simulation of transmitted power of (a) Gaussian and (c) flat-top AWG, (b) Gaussian and (d) flat-top MZI filter. The dashed lines correspond to the measured minimum and maximum VCSEL center wavelengths for all four channels.

3.13 (b)). However, for the flat-top AWG (Figure 3.13 (c)), the loss would be reduced down to 6 dB and for the flat-top cascaded MZI (Figure 3.13 (d)), the VCSEL shift has no impact on the insertion loss. A few devices were manufactured and their experimental performances are reported in Paper [A].

3.4.2 Sensitivity to temperature

As the VCSELs need to operate at temperatures between 25 and at least 60°C, we also decided to compare both the AWG's and the MZI's temperature sensitivity. As the variations of the refractive indices of silicon nitride and silicon dioxide are well known and are around 2.5×10^{-5} /°C for SiN and 0.96×10^{-5} /°C for SiO_2 [50,51], we could deduce

the refractive indices for both materials at 60°C. The refractive index for SiN at 60°C is around 2.0049 and the indices of SiO_2 varies depending on the layer deposition method (thermal, LPCVD or PECVD). As shown in Figure 3.8, the thermal heater for the AWG covers almost the entire device so the refractive indices of the arrayed waveguides are changed. For the MZI however, only a portion of the arm is heated (Figure 3.12) so we changed the indices in the simulation in that portion only. In Figure 3.14 are plotted the simulation results for channel No. 4 (1047 nm) for both devices. The VCSEL temperature shift was also measured and was 2.4 nm for a temperature variation from 25°C to 60°C [16]. The VCSEL center wavelengths at both temperatures are also plotted for comparison.

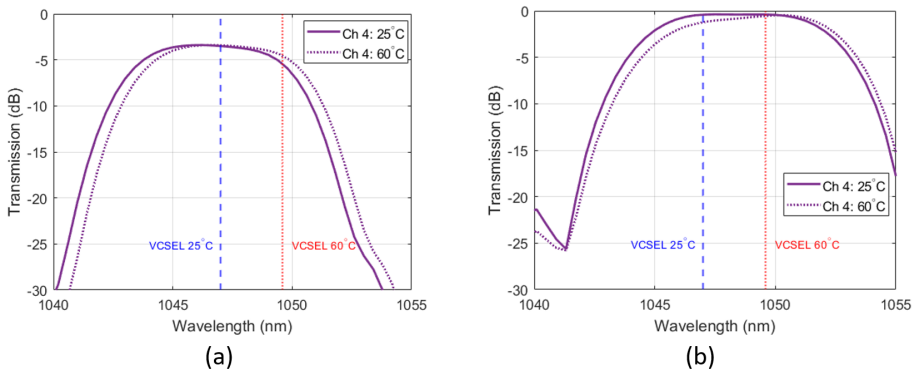

Figure 3.14: Simulation of the sensitivity to temperature of the fourth channel (1047 nm) for (a) the AWG and (b) the MZI filter. The continuous curve corresponds to ambient temperature (25°C) and the dashed curve at 60°C. The positions of the center wavelengths of the VCSEL at both temperatures are also plotted.

We can deduce from the simulations that the AWG and the MZI have a wavelength channel temperature shift of respectively 14.3 pm/°C and 7.7 pm/°C. The AWG is thus twice more sensitive than the MZI according to the simulation. The obtained results are of the same order of magnitude as the experimental results in Ref. [32] which also compare AWGs and MZIs at 1 μm of wavelength, but with a channel separation of 25 nm. However these devices are much less sensitive than the manufactured VCSELs which have a temperature shift of 75 pm/°C approximately. Nevertheless, the flat-top AWG's and MZI's bandwidths are large enough to compensate the VCSEL's high sensitivity to temperature.

3.4.3 Channel accuracy

The impact of the waveguide dimension deviations on the channel accuracy for both technologies is analyzed in this section. We simulated the position of the center wavelength $\Delta\lambda$ when the waveguide width and thickness range respectively from 895 to 905 nm and 155 to 165 nm (Figure 3.15). The target width is 900 nm and the target thickness is 160 nm and the corresponding center wavelength is 1035 nm.

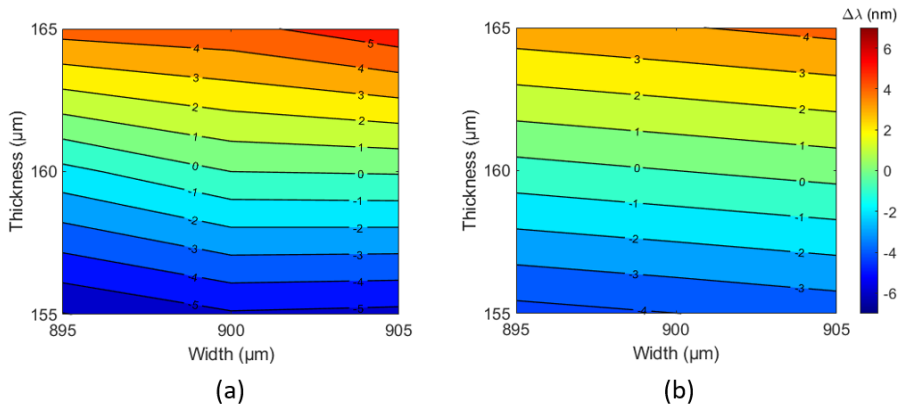

Figure 3.15: Simulation of the wavelength shift when varying the waveguide dimensions for the AWG (a) and the cascaded MZI (b). When $\Delta\lambda = 0$, the center wavelength (1035 nm) is hit.

We see from the simulations that the thickness has a larger impact than the width for both devices, which is logical since this the use of thin singlemode waveguides increases the effective index variation [32]. The simulations reveal that the average wavelength shift per thickness variation is $\Delta\lambda/\mathrm{dt} = 0.984$ nm/nm for the AWG and 0.795 nm/nm for the MZI. In addition, The wavelength shift per nm of width variation is around $\Delta\lambda/\mathrm{dw} = 0.13$ nm/nm for the AWG and 0.075 nm/nm for the MZI. These results are of same order of magnitude as the results in Ref. [32]. The simulations are also realized when the waveguide index is increased by 0.1 % to study the impact of the index variation on the center wavelength for both devices (Figure 3.16). At a wavelength of 1035 nm, we measured an index of 2.004 for LPCVD SiN with the ellipsometry method. An increase of 0.1 % leads to an index of 2.006. The calculated average wavelength shift per percentage of refractive index variation in the SiN waveguide is around 10 nm for the AWG and 6.9 nm for the MZI.

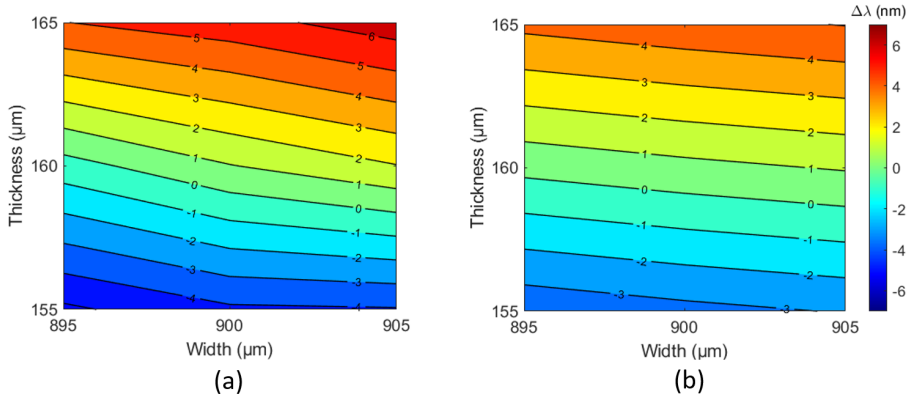

Figure 3.16: Simulation of the wavelength shift when varying the waveguide dimensions and when the SiN core index is increased by 0.1 % for the AWG (a) and the cascaded MZI (b). When $\Delta\lambda = 0$, the center wavelength (1035 nm) is hit.

3.4.4 Footprint with the number of channels

The footprints of the AWG and of the MZI are compared for different channel numbers (4, 8 and 16 channels). The major drawback of the cascaded MZI is that it only can be constructed as a 2^N-channel device (N being the number of stages) [32]. Therefore, the channel number option for the MZI is very limited compared to the AWG for which it is arbitrary. With 4 channels, the wavelength channel spacing is 8 nm. However, if we increase the number of channels (8 or 16), the corresponding VCSEL array will need to have a smaller spacing to ensure a uniform VCSEL array performance. Thus a 8-channel VCSEL array will have a wavelength channel spacing of 4 nm [16]. To go even further, an array of 16 channels would require a spacing of 2 nm, which would be too small considering the precision of the wavelength centers of the VCSELs (Figure 3.13). Therefore, AWGs and MZIs with 8 and 16 channels with channel spacing of respectively 4 nm and 2 nm were designed. For an array of 8 or 16 channels, what would differ in the AWG is the length of the FPRs, the number of output waveguides and of the arrayed waveguides (the base length difference of the arrayed waveguides would be kept the same as for 4 channels). To minimize the insertion loss, the bending radius of the arrayed waveguides should be kept at a minimum of 150 μm. The final estimated sizes of the AWGs would be 1.2 mm^2 and 2.5 mm^2 for 8 and 16 channels respectively. However for the cascaded

MZIs, a device with 8 channels would require 3 stages and a device with 16 channels would have 4 stages. In addition, the base length difference was 36.76 μm for a FSR of 8 nm (4 channels). With the help of Equations 3.6 and 3.7, the base length difference would become 71.52 μm for 8 channels and 143.04 μm for 16 channels. The deduced size of the MZI filters would be approximately 2.3 mm^2 and 6 mm^2 for a system of 8 and 16 channels respectively. The comparison of the size of the two devices are plotted in Figure 3.17.

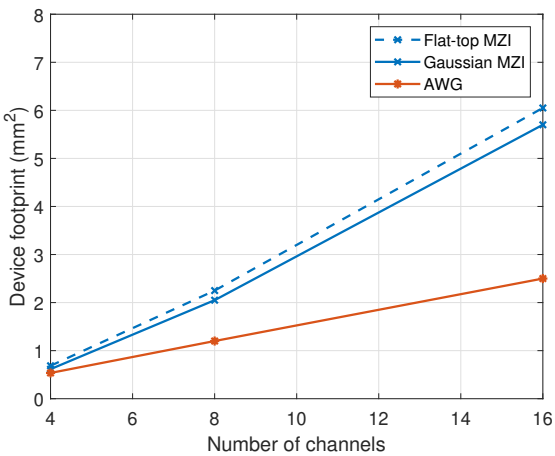

Figure 3.17: Footprint of the AWG and of the cascaded MZI for 4, 8 and 16 channels.

The flat-top and Gaussian AWGs have exactly the same size as the only things that differ between them are the input tapers. The flat-top MZI however needs a second order filter in the first stage while the Gaussian only needs a first order filter (Figure 3.10), which further increases the size of the flat-top design. We can see that the AWG and the MZI have approximately the same size in the case of the system of 4 channels. However, when the number of required channels increases, the MZI is at least twice bigger than the AWG for 16 channels. In conclusion, from a footprint's perspective, the MZI becomes much less interesting than the AWG for a channel number higher than 16 in CWDM demultiplexing.

3.4.5 Insertion loss with the number of channels

In this section are analyzed the insertion losses of the designed AWGs and cascaded MZIs for 4, 8 and 16 channels (Gaussian and flat-top). Additional devices were thus designed for 8 and 16-channel demultiplexers. The transmissions of the Gaussian and flat-top devices are presented in Figures 3.18 and 3.19 respectively.

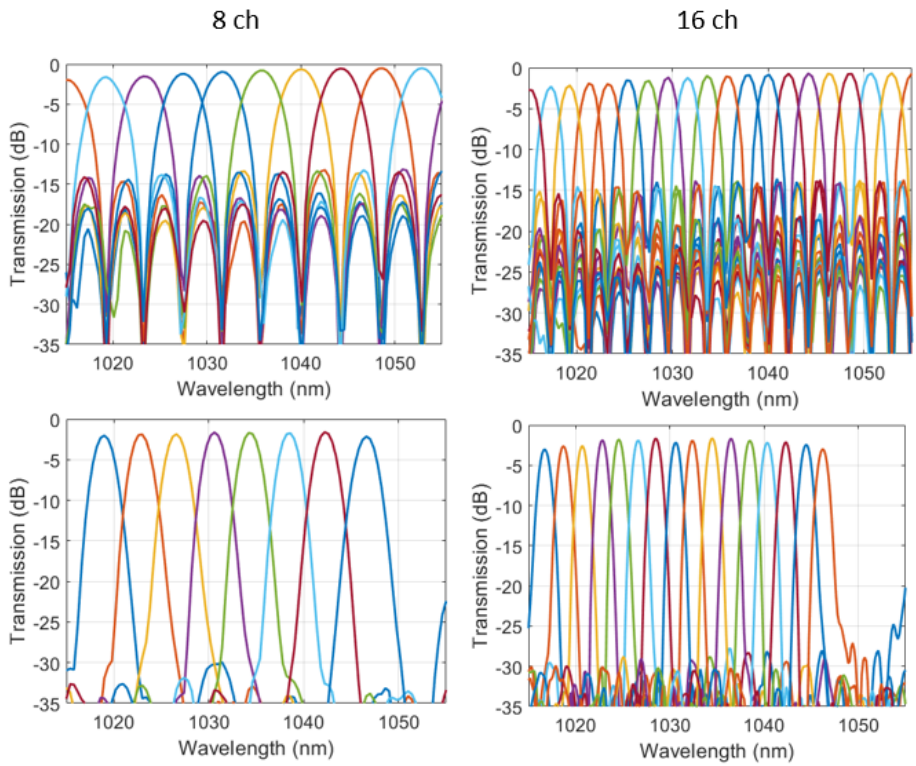

Figure 3.18: Simulated transmissions of Gaussian cascaded MZIs (top) and Gaussian AWGs (bottom) for 8- and 16-channel demultiplexers with 4 nm and 2 nm-channel spacing respectively.

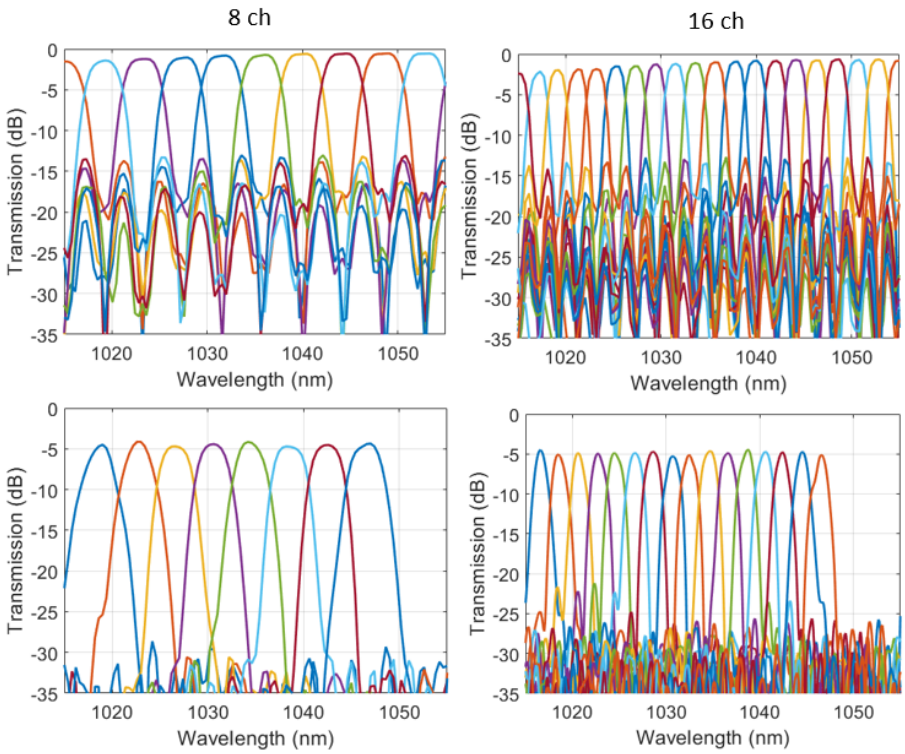

Figure 3.19: Simulated transmissions of flat-top cascaded MZIs (top) and flat-top AWGs (bottom) for 8- and 16-channel demultiplexers with 4 nm and 2 nm-channel spacing respectively.

The average transmission per channel is calculated for each device and is shown in Figure 3.20. In overall, the average transmission seems to decrease with the number of channels as the device increases in size. For the cascaded MZI, the loss is mainly due to the increasing number of MZI filters which reaches 15 for 16 channels. In each stages there are 2 MMIs, each inducing additional coupling loss. As shown in Paper [A], the characterized MMIs had a cross coupling coefficient average of 0.47 at the center wavelength of 1035 nm (the simulated coefficient was 0.495), which corresponds to a coupling loss of 0.28 dB per MMI. The characterized 4-channel flat-top MMI-based cascaded MZI in Paper [A] had an average transmission per channel of -1.18 dB while the simulated in Figure 3.20 was -0.59 dB. It is difficult to estimate the insertion loss of the real devices for the other channel numbers, however for the 16-channel MZI, considering there are 7 MMI splitters in the optical path

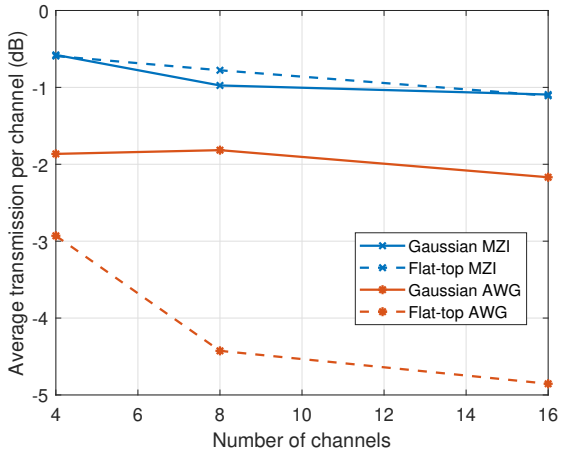

Figure 3.20: Simulated average transmission per channel of the AWG and of the cascaded MZI for 4, 8 and 16 channels.

(each having a coupling loss of 0.28 dB) of each output waveguide, the real transmission could be lower than -2 dB.

The flat-top AWGs have the lowest transmission per channel as it ranges from -3 dB for 4 channels and almost reaches -5 dB for 16 channels. However, the Gaussian AWG seems to be stable at -2 dB on average.

3.4.6 Crosstalk with the number of channels

Crosstalk can be defined as power leakage from one channel to another. There are two kinds of measureable crosstalks, the intrachannel one and the interchannel as illustrated in Figure 3.21.

The interchannel crosstalk can be a combination of side-lobes (yellow and purple curves in Figure 3.21) and of intersection with the adjacent channels (red curve in Figure 3.21)). This type of crosstalk can be compensated prior to detection in the photodetector [52] and therefore is not too significant. However, in the case of cascaded MZIs, it is possible to reduce this type of crosstalk with stage doubling and bent directional couplers [32, 38], but it would also mean designing a much longer device [32].

The intrachannel crosstalk is the signal-noise-ratio between the peak power and the background leaked power from the other channels as shown in Figure 3.21. This type of interference is the most harmful as it has the same wavelength than the signal coming from the VC-

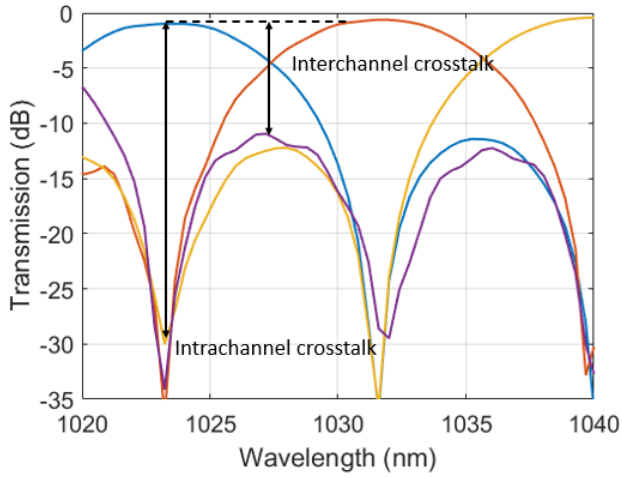

Figure 3.21: Transmission of a 4-channel Gaussian cascaded MZI with the intra- and interchannel crosstalks for the blue channel. The purple curve corresponds to another adjacent channel.

SEL. Therefore it accumulates with the signal coming from the VCSEL corresponding to the channel [53, 54] (the blue channel in Figure 3.21). Furthermore, this type of crosstalk cannot be removed with an optical filter [54]. The bit error rate (BER) is given by [55]:

$$\mathrm{BER} = \frac{1}{2}\mathrm{erfc}\left(\sqrt{\mathrm{SNR}_{\mathrm{tot}}}\right), \tag{3.8}$$

where $\mathrm{SNR}_{\mathrm{tot}}$ is the total signal-to-noise ratio (SNR) that includes the crosstalk XT and is expressed as:

$$\mathrm{SNR}_{\mathrm{tot}} = \left(\frac{1}{\mathrm{SNR}} + \mathrm{XT}\right)^{-1}. \tag{3.9}$$

We estimated with equation 3.9 that a crosstalk of -20 dB would give around a 1 dB-penalty on the SNR at a BER of 10^{-9} (for OOK). Therefore, the maximum intrachannel crosstalk value we would like for our devices is -20 dB. The intrachannel crosstalk is analyzed for the AWGs and MZIs when increasing the number of channels. The average crosstalk per channel is calculated for each device for 4, 8 and 16 channels and the results are plotted in Figure 3.22. We can notice that the flat-top MZI has the highest average crosstalk even reaching -18 dB for 16 channels. However, the Gaussian MZI has a more decent level ranging

from -32 dB for 4 channels to -25 dB for 16 channels. The Gaussian AWG has in overall the lowest level of crosstalk, very close to -30 dB for each number of channels. The flat-top AWG almost has the same level than the flat-top MZI for 4 channels (around -22 dB) but reaches values close to the level of the Gaussian MZI for higher channel numbers.

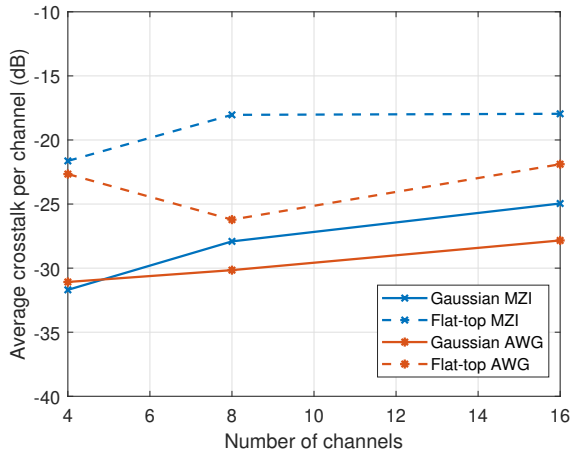

Figure 3.22: Simulated average crosstalk per channel of the AWG and of the cascaded MZI for 4, 8 and 16 channels.

3.5 Conclusions

We saw that the cascaded MZIs based on MMIs (and DCs for the flat-top design) have an average transmitted power close to -1 dB per channel whereas the AWGs have a power close to -2 dB for a Gaussian device and between -3 and -5 dB for a flat-top device. In addition to having a low insertion loss, the Gaussian MZI has a crosstalk lower than -20 dB for each channel number which make this device a good candidate. However, the proposed flat-top MZI has a crosstalk higher than -20 dB for 8 and 16 channels, which is not the case for the flat-top AWG. We can conclude that for a 4-channel demultiplexer, the best candidate is the flat-top cascaded MZI with its high transmission of -0.59 dB and decent average crosstalk of -22 dB. However, for a 8- and 16-channel device, the flat-top MZI's crosstalk becomes higher than the target and a design with either arbitrary cross coupling coefficient MMIs or with bent directional couplers and stage doubling would be required. This means

that amoung the proposed devices for a 8- and 16-channel demultiplexers, the Gaussian cascaded MZI would be the best choice.

CHAPTER 4

Grating couplers

One of the main challenges of silicon photonics is to couple the light from an optical fiber into an integrated on-chip-waveguide while maximizing the optical bandwidth and minimizing the loss. One possibility is to directly couple the light into the input waveguide in the chip-plane with the help of inverse tapers [8] but this generally requires lensed fiber or high numerical apertures to focus the optical beam into the waveguide. Another technology consists in using 3D-taper structures but such tapers require gray scale lithography which is difficult to control and thus potentially lead to fabrication deviation [56, 57]. However, another possibility consists in coupling the light from above the chip with the help of grating structures which collect the fiber mode and couple it into the waveguide. Such structures are either linear or straight and are aproximately 10 to 18 μm wide depending on the size of the fiber mode on top of the chip. Grating couplers are of interest because of their compact size and not requiring polishing facets for coupling [57]. This chapter explores the theoretical aspect of grating couplers, the optimization methods for enhancing the coupling efficiency and compares straight gratings with focusing gratings.

4.1 Theory

The diffraction behavior of a grating coupler is described by the Bragg condition, expressed as [58]:

$$k_0 \sin\Phi + mG = \beta_m, \tag{4.1}$$

where k_0 is the wavevector of the incident beam, Φ the angle of incidence, m the diffraction order, G the grating vector and β_m the propagation constant of the coupled beam into the grating. Then, the grating period Λ can be deduced [59]:

$$\Lambda = \frac{\lambda}{n_{eff} - \sin\Phi}, \tag{4.2}$$

n_{eff} represents the effective index of the grating and λ is the free space wavelength. To avoid strong second order diffraction into the cladding layers and thus loss increment, the fiber is always tilted [59]. With f being the filling ratio of the grating, the grating effective index of the fundamental propagating mode can be expressed as:

$$n_{eff} = f n_{etch,\ eff} + (1 - f) n_{slab,\ eff}, \tag{4.3}$$

The coupling loss of the device is composed with the back reflection of the beam at the top cladding/air interface, the absorption into the Si substrate, the diffracted power into the cladding and the transmitted power. The transmitted power through the waveguide then can be expressed as following [58]:

$$P_{transmitted} = P_{incident} - P_{substrate} - P_{reflection} - P_{out}, \tag{4.4}$$

where $P_{incident}$ is the amount of incident power coming from the fiber, $P_{substrate}$ the amount of power lost into the Si substrate, $P_{reflection}$ the power reflected on the grating coupler and P_{out} the power coupled into the opposite waveguide. Figure 4.1 presents the different losses of a grating coupler.

A large amount of the incident power is reflected on the grating coupler into the air, which limits the coupling efficiency. However, with a top SiO_2 cladding layer, the refractive index contrast is different and the phase matching condition changes too [60]. Therefore, this will cause a reduction of the reflection into the air and increases the coupling efficiency [61] as explained in Figure 4.2.

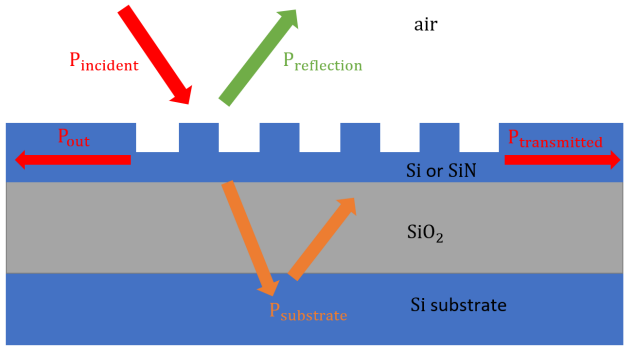

Figure 4.1: Illustration of a grating coupler

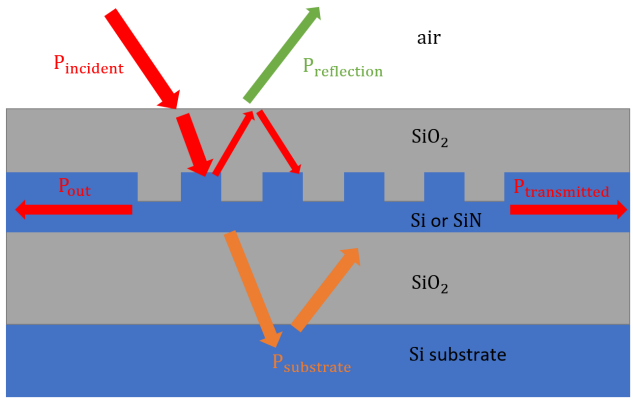

Figure 4.2: Illustration of a grating coupler with a top cladding

4.2 Techniques to improve the coupling efficiency

4.2.1 Apodization

The issue of a uniform grating is that the coupled beam has an exponential decaying power instead of being Gaussian [59, 62]. To reduce the coupling loss, the apodization technique consists in modulating the fill factor or the periodicity along the propagation direction [59]. Then, an even further step called inverse design could be applied to enhance the coupling efficiency and the bandwidth [63].

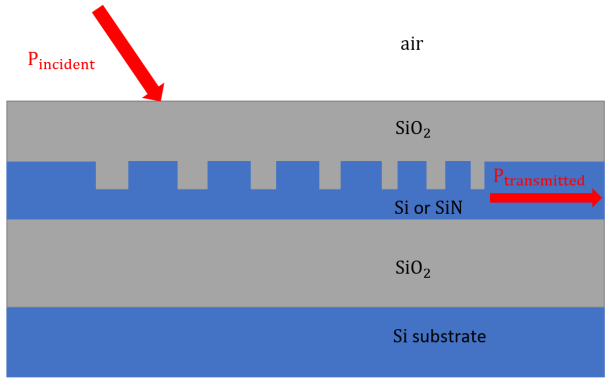

Figure 4.3: Illustration of an appodized grating coupler

4.2.2 Bottom distributed Bragg reflector

A multilayer of distributed Bragg reflector (DBR) placed between the substrate and the buried oxide cladding (BOX) can significantly improve the coupling efficiency. A DBR is a stack of multilayer film with alternate material layers such as SiO_2 and SiN. Such a multilayer stack can be deposited with a sputtering method, LPCVD or using Liquid Source Chemical Vapor Deposition (LSCVD) [64]. A grating coupler based on a SiN waveguide with N = 20 layer SiO_2/SiN DBR with a coupling efficiency of -1.75 dB has been demonstrated [64]. In comparison, a grating coupler without a bottom reflector was manufacured and the measured coupling efficiency was -5 dB [64]. To provide such coupling efficiency, a reflectivity close to 100 % is needed.

4.2.3 Growth overlay

Another method consists in adding a poly-silicon overlay layer on top of the grating prior to the etching. The selected material for the overlay has to induce the required phase change [59]. The advantage of an overlay layer is that it can prevent the need of adding a bottom DBR reflector as demonstrated in [65] with a silicon overlay layer. Indeed, a silicon overlay increases the directionality of the device by creating constructive interference towards the fiber and destructive interference downwards to the silicon substrate [58].

4.2.4 Staircase design

A two-step staircase design also improves the directionality by creating a blazing effect [66, 67]. This innovation consists of a two-step etching of the grating layer and the fiber is placed in the contra-directional coupling configuration as described in [66]. A two-step staircase design is also used in Paper [B]. In Figure 4.4 is shown the difference in coupling efficiency and bandwidth between a conventional and a staircase grating coupler.

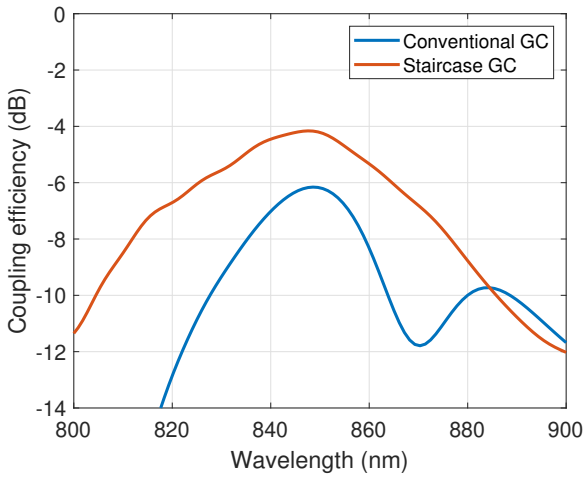

Figure 4.4: 2D FDTD Simulations of coupling efficiency of a conventional GC and a staircase GC for D = 145 μm and $\Phi = 11°$ for the contra-directional case. The grating period are respectively 465 nm and 480 nm for the conventional and the staircase GC.

4.3 Grating couplers for VCSEL arrays at 1 μm

To meet the requirements specified in the first chapter, the grating couplers for all four channels are manufactured in the same chip with a bottom DBR between the Si substrate and the bottom cladding. The material used for the grating coupler is SiN and the waveguide is 160 nm thick. The grating is fully etched as shown in Figure 4.5. All the

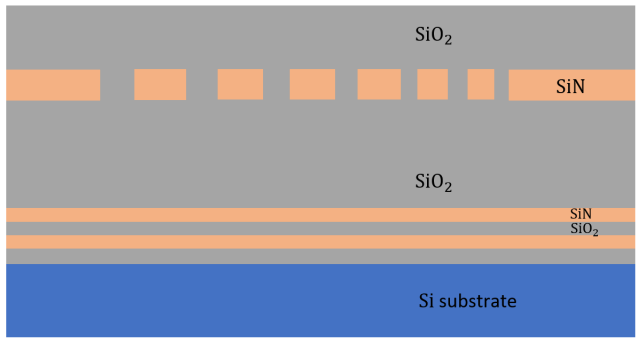

Figure 4.5: Illustration of the apodized DBR-based grating coupler. The real device has 20 grating lines and 6 pairs of SiO_2/SiN bottom layers.

simulations for the grating optimizations are carried out in 2D-FDTD. The initial grating period for each channel is different to meet the Bragg condition in equation 4.2 and each device has 20 grating lines. For the DBR, two material options were available: a DBR based on SiO_2 and SiN or a based on SiO_2 and TiO_2. The TiO_2 material had the advantage over SiN of providing a large bandwidth but one fabrication step included an annealing process, which the TiO_2 material did not survive. Therefore, SiN was finally selected as the second material for the bottom DBR. Figure 4.6 shows the reflectivity of a manufactured 6 pair SiO_2/SiN DBR. The thickness of the SiN and SiO_2 layers of the bottom DBR are respectively 129.117 nm and 178.63 nm.

To optimize the coupling efficiency, a critical control of the top and bottom cladding thicknesses is needed. The top cladding is 2760 nm thick and the bottom cladding is 1850 nm thick. The final step of the coupling efficiency optimization is to apodize the gratings. The length as well the position of each grating line are swept. The final result of the optimized coupling efficiencies of the four channels is presented in Figure 4.7. Channel No. 1 which is optimized for a target wavelength of 1023 nm presents the lowest coupling efficiency (-1.5 dB) while having

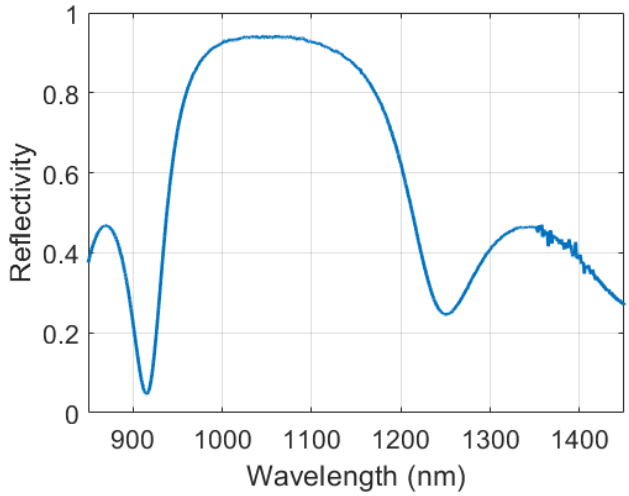

Figure 4.6: Measured reflectivity of a 6 pair SiO_2/SiN DBR. The measured peak reflectivity is 0.94.

the largest bandwidth. The highest efficiency obtained is -1 dB with channel No. 3. at 1039 nm.

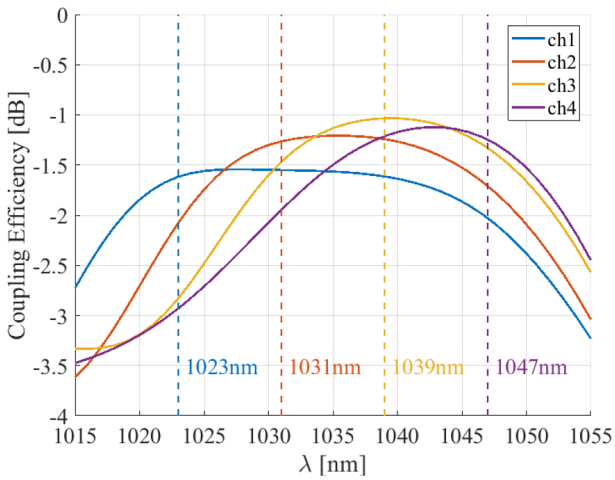

Figure 4.7: 2D-FDTD Simulations of coupling efficiency of the channel array.

4.4 Types of grating couplers

4.4.1 Linear gratings

Typical straight grating couplers have a grating section that is between 15 and 30 μm long and 10 to 18 μm wide to collect 100 % of the incoming beam from the fiber/VCSEL. The light is then coupled into a slab-waveguide that is as wide as the grating and finally converted into the single-mode waveguide with either a linear or an adiabatic taper. Typical tapers are around 400 μm long to minimize the radiation loss and have a conversion efficiency around 98 %. An example of a straight grating coupler is proposed in Paper [B] in which the grating section is 10 μm wide and between 17 and 21 μm. The taper of the device is 300 μm long. In Figure 4.8 we show the conversion efficiency of the linear taper converting the mode from the 12 μm wide slab-waveguide to the 0.9 μm wide single mode waveguide.

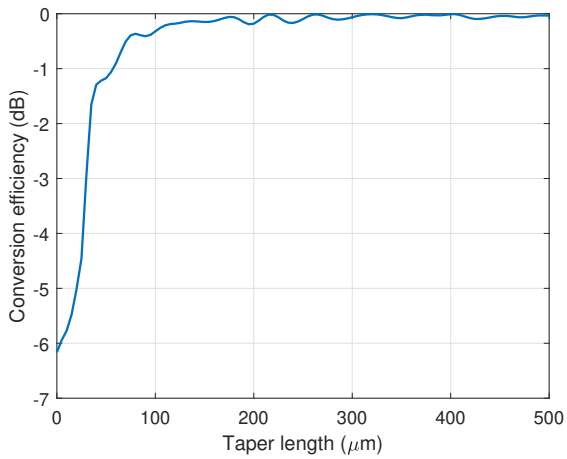

Figure 4.8: EME Simulation of the conversion efficiency of a linear taper. The slab-waveguide is 12 μm wide and the output waveguide 0.9 μm wide for a thickness of 160 nm.

From the EME simulation, a taper length of 175 μm seems to be enough, but a length of 400 μm is often preferred since the coupled VCSEL mode does not fully match the fundamental TE slab-mode. Such grating couplers are very efficient but have a large footprint due to their ultra-long conversion tapers. However, ultra-short tapers with conversion efficiencies of 96 % have been demonstrated at 1550 nm on Si-

waveguides [68].

4.4.2 Focusing gratings

Another way to reduce the size of the grating coupler while keeping a decent coupling efficiency consists in curving the grating lines so that the incoming beam is focused into the taper. The curvature is calculated with following equation [58, 69]:

$$q\lambda = xn_{cladding}cos\theta - n_{eff}\sqrt{y^2 + x^2}, \tag{4.5}$$

where q is the grating line number, x the coordinate of the propagation direction and y the coordinate in the lateral direction, n_{eff} the effective index of the coupled mode, $n_{cladding}$ the refractive index of the top cladding (or air if there is no cladding) and θ the coupling angle. The device (taper included) will have a length of approximately 40 μm or 10 times smaller than a conventional straight grating coupler. Figure 4.9 shows a drawing of a focusing grating coupler.

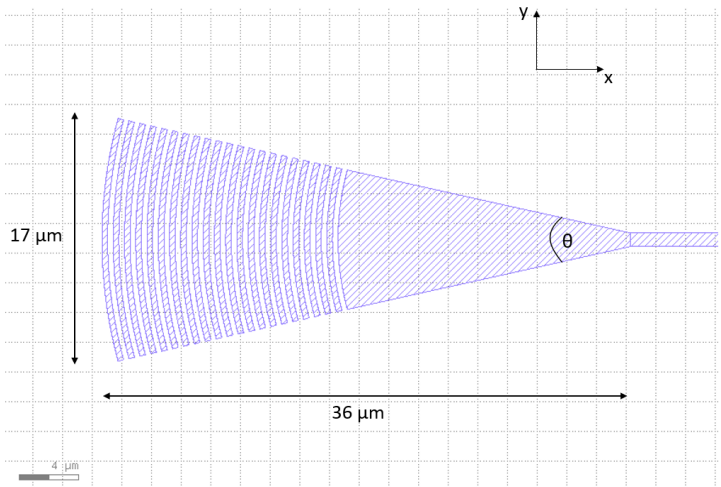

Figure 4.9: Designed focusing grating coupler in a gds file.

The positions of the grating lines of the apodized grating couplers simulated in 2D-FDTD are then implemented into the focusing designs in 3D-FDTD. In Figure 4.10 is the simulation result of the apodized focusing grating coupler corresponding to channel No. 3 (1039 nm).

The coupling efficiency at 1039 nm reached -1.5 dB, which is still within the target efficiency (power budget for the grating couplers: -2 dB). The device also has a 3 dB-bandwidth of 39 nm.

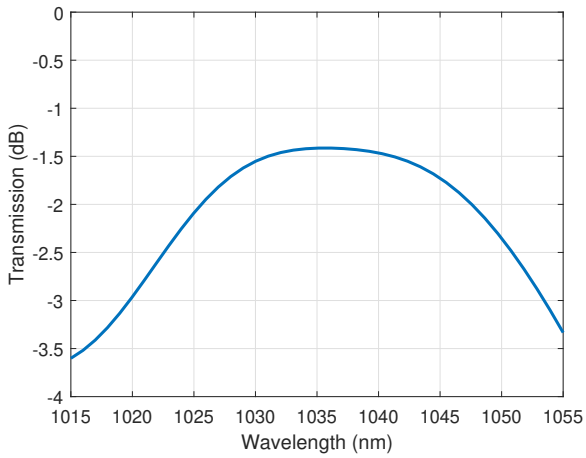

Figure 4.10: 3D-FDTD simulation of the coupling efficiency of an apodized focusing grating coupler (channel 3: 1039 nm) with a bottom DBR.

CHAPTER 5

Conclusions and future outlook

This thesis was mainly focusing on demultiplexing technologies and grating couplers. In this chapter we discuss future works and the research aspects that need to be completed.

Paper [A] is in preparation and the last section (CWDM at 1 μm) of chapter 3 will be appended later for the simulations and analysis aspects. The experimental sensitivity to temperature change of the AWG and the MZI still needs to be investigated. In this thesis, we compared AWGs with cascaded MZIs in terms of insertion loss, crosstalk, footprint with the number of output channels as well as their sensitivity to temperature and to small variation of waveguide dimension. Only 4-channel devices were manufactured and the flat-top MMI/DC-based MZI is a good option for its low insertion loss and signal flatness and the Gaussian MMI-based MZI has the lowest crosstalk (-18.7 dB demonstrated in Paper [A]). As a crosstalk of -20 dB per channel is required, the Gaussian cascaded MZI may be good enough for our 4-channel transmitter. In future designs, MZI with either bent directional couplers or arbitrary cross coupling coefficient could be explored. Indeed, due to the low wavelength dependence of their power splitters, low crosstalk level can be obtained as demonstrated in [38, 45]. Finally, MZIs equipped with phase shifters to make them more tolerant to fabrication deviations could later be explored.

Chapter 4 sets a preliminary work on DBR-based apodized grating

couplers (both linear and focusing) for a 4-VCSEL array and will be developed in a near future. A few devices are already manufactured without a bottom DBR and need to be tested. Several chips with manufactured SiO_2/Si_3N_4 are ready and will later be used to complete the fabrication with new high efficiency grating couplers.

Finally, an integrated DWDM multi-layer transmitter at 1550 nm is being developed. This transmitter includes a soliton comb source with a spacing of 100 GHz (0.8 nm) followed by a 9-channel 100 GHz AWG. These component are based on thin Si_3N_4 waveguides (200 nm) and the output channels of the AWG are modulated into a $LiNbO_3/Si_3N_4$-bilayer vertical coupler.

CHAPTER 6

Summary of papers

Paper A
Arrayed Waveguide Grating and MZI Filters for Wavelength Division (De-)Multiplexing at 1 μm
In preparation.

This paper presents a comparison of an AWG with different types of cascaded MZIs. The MZI components are either based on directional couplers, MMIs or even both to obtain a flat-top transmission while keeping a low crosstalk level.

My contribution: I did all the designs of the devices as well the simulations and the measurements. I also wrote a first version of the paper.

Paper B
Angled Flip-Chip Integration of VCSELs on Silicon Photonic Integrated Circuits
Journal of Lightwave Technology, Vol. 40, No. 15, pp. 5190-5200, August 1, 2022. DOI: 10.1109/JLT.2022.3172781
This article demonstrates a complete silicon photonic integrated circuit with a flip-chiped singlemode 850 nm VCSEL at the input and a photodiode (PD) at the output. We investigated the coupling efficiency of

the grating couplers and the optical feedback on the VCSEL or in other words the amount of reflected light on the VCSEL aperture in the contra- and the codirectional configurations. The transmission is measured in different scenarios: VCSEL-PD, VCSEL-singlemode fiber and VCSEL-multimode fiber.

My contribution: I did all the simulations of the coupling efficiencies in every configuration (contra- and co-directional) for each VCSEL angle and dimension as well as the simulation of the optical feedback. I also wrote the second half of section II, all the section III and partially section IV. I also added the modifications required by the reviewers.

References

[1] "https://www.itu.int/pub/r-rep-m.2370."

[2] F. Tariq, M. R. A. Khandaker, K.-K. Wong, M. A. Imran, M. Bennis, and M. Debbah, "A speculative study on 6G," *IEEE Wireless Communications*, vol. 27, no. 4, 2020.

[3] "https://digital-strategy.ec.europa.eu/en/library/energy-efficient-cloud-computing-technologies-and-policies-eco-friendly-cloud-market."

[4] statistica, "https://www.statista.com/statistics/633826/worldwide-hyperscale-data-center-numbers/."

[5] "https://www.rankred.com/largest-data-centers-in-the-world/."

[6] E. Simpanen, J. Gustavsson, E. Haglund, E. Haglund, A. Larsson, W. Sorin, S. Mathai, and M. Tan, "1060 nm single-mode vertical-cavity surface-emitting laser operating at 50 Gbit/s data rate," *Electronics letters*, vol. 53, no. 13, pp. 869–871, 2017.

[7] A. Larsson, E. Simpanen, J. Gustavsson, E. Haglund, E. Haglund, T. Lengyel, P. Andrekson, W. Sorin, S. Mathai, M. Tan, and S. Bickham, "1060 nm VCSELs for long-reach optical interconnects," *Elsevier Optical Fiber Technology*, vol. 44, pp. 36–42, 2018.

[8] X. Hu, M. Girardi, Z. Ye, P. Muñoz, A. Larsson, and V. Torres-Company, "Si3N4 photonic integration platform at 1 μm for optical interconnect," *Optics express*, vol. 28, no. 9, pp. 13 019–13 031, 2020.

[9] D. Mahgerefteh, C. Thompson, C. Cole, G. Denoyer, T. Nguyen, I. Lyubomirsky, C. Kocot, and J. Tatum, "Techno-economic comparison of silicon photonics and multimode vcsels," *Journal of Lightwave Technology*, vol. 34, no. 2, pp. 233–242, 2016.

[10] M.-J. Li, "Novel optical fibers for data center applications," in *Proceedings of SPIE*, San Francisco, California, United States, 2016.

[11] "Spectral-dependent electronic-photonic modeling of high-speed vcsel-mmf links for optimized launch conditions," *Optics express*, vol. 29, no. 2, pp. 2738–2756, 2021.

[12] A. Larsson, J. S. Gustavsson, E. Haglund, E. P. Haglund, E. Simpanen, and T. Lengyel, "VCSEL modulation speed: status and prospects," in *Proceedings of SPIE*, San Francisco, California, United States, 2019.

[13] P. Westbergh, J. S. Gustavsson, A. Larsson, T. F. Taunay, L. Bansal, and L. Grüner-Nielsen, "Crosstalk characteristics and performance of VCSEL array for multicore fiber interconnects," *IEEE Journal of Selected Topics in Quantum Electronics*, vol. 21, no. 6, pp. 429–435, 2015.

[14] D. L. Butler, M.-J. Li, S. Li, Y. Geng, R. R. Khrapko, R. A. Modavis, V. N. Nazarov, and A. V. Koklyushkin, "Space division multiplexing in short reach optical interconnects," *Journal of Lightwave Technology*, vol. 35, no. 4, pp. 677–682, 2017.

[15] E. Haglund, M. Jahed, J. S. Gustavsson, A. Larsson, J. Goyvaerts, R. Baets, G. Roelkens, M. Rensing, and P. O´Brien, "High-power single transverse and polarization mode vcsel for silicon photonics integration," *Optics express*, vol. 27, no. 13, pp. 18 892–18 899, 2019.

[16] M. Jahed, J. S. Gustavsson, and A. Larsson, "VCSEL wavelength setting by intra-cavity phase tuning - numerical analysis and experimental verification," *IEEE Journal of Quantum Electronics*, vol. 57, no. 6, pp. 1–7, 2021.

[17] R. Baets, A. Z. Subramanian, S. Clemmen, B. Kuyken, P. Bienstman, N. L. Thomas, G. Roelkens, D. V. Thourhout, P. Helin, and S. Severi, "Silicon photonics: silicon nitride vs silicon-on-insulator," in *Optical Fiber Communications Conference and Exhibition (OFC)*, Anaheim, CA, USA, 2016.

[18] Y. Su, Y. Zhang, C. Qiu, X. Guo, and L. Sun, "Silicon photonic platform for passive waveguide devices: Materials, fabrication, and applications," *Advanced Materials Technologies*, vol. 5, no. 8, 2020.

[19] B. S. Ahluwalia, Ø. I. Helle, and O. G. Hellesø, "Rib waveguides for trapping and transport of particles," *Optics Express*, vol. 24, no. 5, pp. 4477–4487, 2016.

[20] N. Eti and H. Kurt, "Model analysis of ridge and rib types of silicon waveguides with void compositions," *IEEE Journal of Quantum Electronics*, vol. 52, no. 10, 2016.

[21] T. H. Talukdar, G. D. Allen, I. Kravchenko, and J. D. Ryckman, "Single-mode porous silicon waveguide interferometers with unity confinement factors for ultra-sensitive surface adlayer sensing," *Optics express*, vol. 27, no. 16, pp. 22 485–22 498, 2019.

[22] M. Zhang, G.Hu, S. Zhang, D. Gao, Y. Sun, and F. Wang, "Gain characteristics of the hybrid slot waveguide amplifiers integrated with NaYF4:Er3+ NPs-PMMA covalently linked nanocomposites," *Royal society of chemistry*, vol. 10, no. 19, pp. 11 148–11 155, 2020.

[23] S. Roberts, X. Ji, J. Cardenas, M. Corato-Zanarella, and M. Lipson, "Measurements and modeling of atomic-scale sidewall roughness and losses in integrated photonic devices," *Advanced Optical Materials*, no. 2102073, 2022.

[24] J. F. Bauters, M. J. R. Heck, D. John, D. Dai, M.-C. Tien, J. S. Barton, A. Leinse, R. G. Heideman, D. J. Blumenthal, and J. E. Bowers, "Ultra-low-loss high-aspect-ratio (Si3N4) waveguides," *Optics Express*, vol. 19, no. 4, pp. 3163–3174, 2011.

[25] *www.lumerical.com/learn/whitepapers/lumericals-2-5d-fdtd-propagation-method/.*

[26] P. Muñoz, D. Pastor, and J. Capmany, "Modeling and design of arrayed waveguide gratings," *Journal of Lightwave Technology*, vol. 20, no. 4, pp. 661–674, 2002.

[27] N. Ismail, F. Sun, G. Sengo, K. Wörhoff, A. Driessen, R. M. de Ridder, and M. Pollnau, "Improved arrayed-waveguide-grating layout avoiding systematic phase errors," *Optics express*, vol. 19, no. 9, pp. 8781–8794, 2011.

[28] R. Marz, "Dense wavelength division multiplex: Research activities at siemens," in *Proceedings of SPIE*, Beijing, China, 1996.

[29] Y. Hibino, "Recent advances in high-density and large-scale AWG multi/demultiplexers with higher index-contrast silica-based PLCs," *IEEE Journal of Selected Topics of Quantum Electronics*, vol. 8, no. 6, pp. 1090–1101, 2002.

[30] D. Dai and J. E. Bowers, "Silicon-based on chip multiplexing technologies and devices for peta-bit optical interconnects," *Nanophotonics de Gruyter*, vol. 3, no. 4-5, pp. 283–311, 2013.

[31] P. Pan, J. An, J. Zhang, Y. Wang, H. Wang, L. Wang, X. Yin, Y. Wu, J. Li, Q. Han, and X. Hu, "Flat-top awg based on inp deep ridge waveguide," *Elsevier Optical Communications*, vol. 255, pp. 376–381, 2015.

[32] S. S. Cheung and M. R. T. Tan, "Silicon nitride (Si3N4) (de-)multiplexers for 1-μm CWDM optical interconnects," *Journal of Lightwave Technology*, vol. 38, no. 13, pp. 3404–3413, 2020.

[33] A. A. Bernussi, L. G. de Peralta, V. Gorbounov, J. A. Linn, S. Frisbie, R. Gale, and H. Temkin, "Mirror quality and the performance of reflective arrayed-waveguide grating multiplexers," *Journal of Lightwave Technology*, vol. 22, no. 7, pp. 1828–1832, 2004.

[34] D. Dai and S. He, "Compact silicon-based wavelength-selective photonic integrated devices and the applications," in *Proceedings of SPIE*, San Jose, California, United States, 2009.

[35] W. Bogaerts, S. K. Selvaraja, P. Dumon, J. Brouckaert, K. D. Vos, D. V. Thourhout, and R. Baets, "Silicon-on-insulator spectral filters fabricated with cmos technology," *Journal of Selected Topics in Quantum Electronics*, vol. 16, no. 1, pp. 33–44, 2010.

[36] J.-J. He, B. Lamontage, A. Delâge, L. Erickson, M. Davies, and E. S. Koteles, "Monolithic integrated wavelength demultiplexer based on a waveguide rowland circle grating in InGaAsP/InP," *Journal of Lightwave Technology*, vol. 16, no. 4, pp. 631–638, 1998.

[37] F. Horst, W. M. J. Green, S. Assefa, S. M. Shank, Y. A. Vlasov, and B. J. Offrein, "Cascaded mach-zehnder wavelength filters in silicon photonics for low loss and flat pass-band WDM (de-)multiplexing," *Optics express*, vol. 21, no. 10, pp. 11 652–11 658, 2013.

[38] H. Xu and Y. Shi, "Flat-top CWDM (de)multiplexer based on MZI with bent directional couplers," *IEEE Photonics Technology Letters*, vol. 30, no. 2, 2018.

[39] J. C. Mikkelsen, A. Bois, T. Lordello, D. Mahgerefteh, S. Menezo, and J. K. S. Poon, "Polarization-insensitive silicon nitride mach-zehnder lattice wavelength demultiplexers for cwdm in the o-band," *Optics express*, vol. 26, no. 23, pp. 30 076–30 084, 2018.

[40] D. Liu, M. Zhanh, Y. Shi, and D. Dai, "Four-channel CWDM (de)multiplexers using cascaded multimode waveguide gratings," *IEEE Photonics Technology Letters*, vol. 32, no. 4, 2020.

[41] D. Liu, H. Wu, and D. Dai, "Silicon multimode waveguide grating filter at 2 μm," *Journal of Lightwave Technology*, vol. 37, no. 10, pp. 2217–2222, 2019.

[42] Y. Tang, H. Wu, S. Wang, C. Li, and D. Dai, "Silicon-based hybrid demultiplexer for wavelength- and mode-division multiplexing," *Optics Letters*, vol. 43, no. 9, pp. 1962–1965, 2018.

[43] P. Chen, S. Chen, X. Guan, Y. Shi, and D. Dai, "High-order microring resonators with bent couplers for a box-like filter response," *Optics Letters*, vol. 39, no. 21, pp. 6304–6307, 2014.

[44] F. Xia, M. Rooks, L. Sekaric, and Y. Vlasov, "Ultra-compact high order ring resonator filters using submicron silicon photonic wires for on chip optical interconnect," *Optics express*, vol. 15, no. 19, pp. 11 934–11 941, 2007.

[45] M. Cherchi, F. Sun, M. Kapulainen, M. Harjanne, and T. Aalto, "Flat-top interleavers based on single mmis," in *SPIE OPTO*, San Francisco, California, United States, 2020.

[46] "Design and analysis of low loss MMI based 4x4 optical switch using benes architecture with SOAs," *2008 IEEE Photonics-Global@Singapore*, 2008.

[47] Y. Hibino, "Recent advances in high-density and large-scale AWG multi/demultiplexers with higher index-contrast silica-based PLCs," *IEEE Journal of Selected Topics in Quantum Electronics*, vol. 8, no. 6, pp. 1090–1101, 2002.

[48] M. K. Smit and C. van Dam, "PHASAR-based WDM-devices: Principles, design and applications," *IEEE Journal of Selected topics in Quantum Electronics*, vol. 2, no. 2, pp. 236–250, 1996.

[49] F. Horst, W. M. J. Green, S. Assefa, S. M. Shank, Y. A. Vlasov, and B. J. Offrein, "Cascaded Mach-Zehnder wavelength filters in silicon photonics for low loss and flat pass-band WDM (de-)multiplexing," *Optics express*, vol. 21, no. 10, pp. 11 652–11 658, 2013.

[50] A. Arbabi and L. L. Goddard, "Measurements of the refractive indices and thermo-optic coefficients of Si3N4 and SiOx using microring resonances," *Optics Letters*, vol. 38, no. 19, pp. 3878–3881, 2013.

[51] A. W. Elshaari, I. E. Zadeh, K. D. Jöns, and V. Zwiller, "Thermo-optic characterization of silicon nitride resonators for cryogenic photonic circuits," *IEEE Photonics Journal*, vol. 8, no. 3, 2016.

[52] F. Alishahi, A. Mohajerin-Ariaei, A. Fallahpour, Y. Cao, A. Almaiman, P. Liao, C. Bao, B. Shamee, K. Zou, H. Zhou, A. N. Willner, J. D. Touch, M. Tur, C. Langrock, M. M. Fejer, and A. E. Willner, "Optical mitigation of interchannel crosstalk for multiple spectrally overlapped 20 gbaud QPSK/16-QAM WDM channels using nonlinear wave mixing," *Journal of Lightwave Technology*, vol. 37, no. 2, pp. 548–554, 2019.

[53] J. Zhou, R. Cadeddu, E. Casaccia, C. Cavazzoni, and M. J. O´Mahony, "Crosstalk in multiwavelength optical cross-connect networks," *Journal of Lightwave Technology*, vol. 14, no. 6, pp. 1423–1435, 1996.

[54] T. Gyselings, G. Morthier, and R. Baets, "Crosstalk analysis of multiwavelength optical cross connects," *Journal of Lightwave Technology*, vol. 17, no. 8, pp. 1273–1283, 1999.

[55] M. I. Basudewa, Z. H. Bagaskara, S. S. A. Damita, R. F. Putra, and D. Ahmadi, "Bit error rate performance analysis for free space optic communication," in *IOP Conference Series: Materials Science and Engineering*, 2020.

[56] A. Sure, T. Dillon, J. Murakowski, C. Lin, D. Pustai, and D. W. Prather, "Fabrication and characterization of three-dimensional silicon tapers," *Optics express*, vol. 11, no. 26, pp. 3555–3561, 2003.

[57] G. Roelkens, D. V. Thourhout, and R. Baets, "High efficiency silicon-on-insulator grating coupler based on a poly-silicon overlay," *Optics express*, vol. 14, no. 24, pp. 11 622–11 630, 2006.

[58] L. Cheng, S. Mao, Z. Li, Y. Han, and H. Y. Fu, "Grating couplers on silicon photonics: Design principles, emerging trends and practical issues," *MPDI Micromachines*, vol. 11, no. 666, 2020.

[59] S. Nambiar, P. Sethi, and S. K. Selvaraja, "Grating-assisted fiber to chip coupling for SOI photonic circuits," *MPDI Applied Sciences*, vol. 8, no. 1142, 2018.

[60] D. Marris-Morini, X. L. Roux, L. Vivien, E. Cassan, D. Pascal, M. Halbwax, S. Maine, and S. Laval, "Optical modulation by carrier depletion in a silicon pin diode," *Optics express*, vol. 14, no. 22, pp. 10 838–10 843, 2006.

[61] G. Maire, L. Vivien, G. Sattler, A. Kaźmierczak, B. Sanchez, K. B. Gylfason, A. Griol, D. Marris-Morini, E. Cassan, D. Giannone, H. Sohlström, and D. Hill, "High efficiency silicon nitride surface grating couplers," *Optics express*, vol. 16, no. 1, pp. 328–333, 2008.

[62] Y. Wang, H. Yun, Z. Lu, R. Bojko, W. Shi, X. Wang, J. Flueckiger, F. Zhang, M. Caverley, N. A. F. Jaeger, and L. Chrostowski, "Apodized focusing fully etched subwavelength grating couplers," *IEEE Photonics Journal*, vol. 7, no. 3, 2015.

[63] N. V. Sapra, D. Vercruysse, L. Su, K. Y. Yang, J. Skarda, A. Y. Piggott, and J. Vučković, "Inverse design and demonstration of broadband grating couplers," *IEEE Journal of Selected Topics in Quantum Electronics*, vol. 25, no. 3, pp. 1–7, 2019.

[64] J. Hong, A. M. Spring, F. Qiu, and S. Yokoyama, "A high efficiency silicon nitride waveguide grating coupler with a multilayer bottom reflector," *Scientific Reports*, vol. 9, no. 12988, 2019.

[65] D. Vermeulen, S. Selvaraja, P. Verheyen, G. Lepage, W. Bogaerts, P. Absil, D. V. Thourhout, and G. Roelens, "High-efficiency fiber-to-chip grating couplers realized using an advanced cmos-compatible silicon-on-insulator platform," *Optics express*, vol. 18, no. 17, pp. 18 278–18 283, 2010.

[66] Y. Chen, R. Halir, I. Molina-Fernańdez, P. Cheben, and J.-J. He, "High-efficiency apodized-imaging chip-fiber grating coupler for silicon nitride waveguides," *Optics Letters*, vol. 41, no. 21, pp. 5059–5062, 2016.

[67] Y. Chen, T. Bucio, A. Z. Khokhar, M. Banakar, K. Grabska, F. Y. Gardes, R. Halir, I. Molina-Fernańdez, P. Cheben, and J.-J. He, "Experimental demonstration of an apodized-imaging chip-fiber grating coupler for Si3N4 waveguides," *Optics Letters*, vol. 42, no. 18, pp. 3566–3569, 2017.

[68] P. Sethi, A. Haldar, and S. K. Selvaraja, "Ultra-compact low-loss broadband waveguide taper in silicon-on-insulator," *Optics express*, vol. 25, no. 9, pp. 10 196–10 203, 2017.

[69] F. V. Laere, W. Bogaerts, D. V. T. D. Taillaert, P. Dumon, and R. Baets, "Compact focusing grating couplers between optical fibers and silicon-on-insulator photonic wire waveguides," in *Optical Fiber Communications Conference and Exhibition (OFC)*, Anaheim, CA, USA, 2007.